WILEY-VCH

DOI: 10.1002

Article type: Full Paper

Switchable Chiral Mirrors

Meng Liu,[#] Eric Plum,[#], Hua Li, Siyu Duan, Shaoxian Li, Quan Xu, Xueqian Zhang, Caihong Zhang, Chongwen Zou, Biaobing Jin, Jiaguang Han,* and Weili Zhang**

[#]M. Liu and E. Plum contributed equally to this work

M. Liu, S.-X. Li, Dr. Q. Xu, Dr. X.-Q. Zhang, Prof. J.-G. Han, Prof. W.-L. Zhang
Center for Terahertz Waves and College of Precision Instrument and Optoelectronics Engineering, Tianjin University, Tianjin 300072, China
E-mail: jiaghan@tju.edu.cn

Dr. E. Plum
Centre for Photonic Metamaterials & Optoelectronics Research Centre, Zepler Institute, University of Southampton, Southampton, SO17 1BJ, UK.
E-mail: erp@orc.soton.ac.uk

H. Li, S.-Y. Duan, Prof. C.-H. Zhang, Prof. B.-B Jin,
Research Institute of Superconductor Electronics (RISE), School of Electronic Science and Engineering, Nanjing University, Nanjing 210093, P. R. China

Prof. C.-W. Zou
National Synchrotron Radiation Laboratory, University of Science & Technology of China, Hefei 230029, P. R. China

Prof. W.-L. Zhang
School of Electrical and Computer Engineering, Oklahoma State University, Stillwater, Oklahoma 74078, USA
E-mail: weili.zhang@okstate.edu

Keywords

chirality, mirror, phase transition, circular conversion dichroism, metamaterial

Mirrors are widely used for redirection of electromagnetic waves in optical systems, making them arguably the most irreplaceable optical component. Metamaterial-based chiral mirrors,

composed of a 2D-chiral planar metallic structure backed by a conventional mirror, reflect one circular polarization without changing its handedness, while absorbing the other. Here we demonstrate three types of switchable chiral mirror. We realize switching from a chiral mirror to either a conventional mirror, a handedness-preserving mirror, or a chiral mirror of opposite handedness. These advances are underpinned by switching the handedness of 2D-chiral metamaterial and the associated effect of circular conversion dichroism, which we report here for the first time. Switching is achieved by exploiting the temperature-activated dielectric-to-metal phase transition of vanadium dioxide to modify the symmetry and chirality of the metamaterial's resonators. Current distributions explain the temperature-controlled optical properties by handedness-selective excitation of reflective electric dipole and absorbing magnetic dipole modes.

1. Introduction

Mirrors change the propagation direction of electromagnetic waves, making them essential for applications across the electromagnetic spectrum, e.g. imaging, lasers and communications. Common examples of mirrors are metallic films, interference-based dielectric multilayers, Bragg reflectors and Faraday rotator mirrors.[1] Conventional isotropic mirrors reflect linear polarization without polarization change; however, they will change left-handed circular polarization (LCP) into right-handed circular polarization (RCP), and vice versa. Thus, the ultimate handedness of a circularly polarized wave reflected by conventional isotropic mirrors is determined by the number of reflections. Metamaterial-based mirrors can avoid this deficiency by providing handedness-preserving reflection of either one[2] or both circular polarizations.[3, 4] Handedness-preserving reflection

of both circular polarizations is achieved by placing an anisotropic structure – a metamaterial or a quarter wave plate – in front of a conventional mirror. Handedness-preserving reflection of only one circular polarization and absorption of the other is achieved by a chiral mirror. It is composed of a two-dimensionally chiral (2D-chiral) planar metamaterial backed by a conventional mirror.[5-13] Chiral mirrors have already enabled polarization-sensitive near-infrared detectors,[14] multiplexed holograms for circularly polarized waves,[15] chiral second harmonic generation[16] and nonlinear all-optical polarization modulation[17]. They could also lead to circularly polarized lasers and Fabry-Perot cavities with enhanced tunability, as well as enhanced spectroscopies of chiral media.[2] So far, the type of mirror – conventional, handedness-preserving or chiral – is determined at the time of fabrication. Switching between different types of mirror would require real-time control over symmetry and chirality of a metamaterial-based mirror. Dynamic control over metamaterial properties can be achieved by either changing the geometry of the metamaterial structure[18-23] (e.g. by actuation) or by changing the electromagnetic properties of metamaterial components, e.g. substrate,[24,25] continuous[26-31] or structured[32-43] functional layers in combination with metal resonators, or resonators made of functional material (e.g. through phase transitions).[44-47]

Here we demonstrate three types of switchable chiral mirror (**Figure 1**). We realize temperature-activated switching of an LCP mirror (a) to a conventional mirror (b), a handedness-preserving mirror (c), and an RCP mirror (d). The LCP mirrors consist of a 2D-chiral metallic metamaterial separated from a conventional metallic mirror by a dielectric spacer. Switching is achieved by exploiting the dielectric-to-metal phase transition[47-49] of additional vanadium dioxide (VO_2) inclusions to change the symmetry of the metamaterial.

Upon heating, the symmetry of the chiral anisotropic metamaterial changes to achiral isotropic, achiral anisotropic or chiral with opposite handedness, resulting in the above switchable mirror functionalities at terahertz frequencies. In the next section, we will report such switching of the handedness of 2D-chiral metamaterial and the associated effect of circular conversion dichroism for the first time. Thereafter, we will exploit this functionality to realize switchable chiral mirrors. Such active chiral mirrors have sub-wavelength thickness and can be applied to control reflection, absorption and polarization of electromagnetic waves, e.g. to realize cavities and lasers that can be switched between differently polarized modes. We note that optical switching of vanadium dioxide with picosecond optical pulses has been reported, indicating that switchable chiral mirrors could be fast.[50]

2. Results and Discussion

2.1 Switching 2D Chirality and Circular Conversion Dichroism

Any structure that is different from its mirror image is said to be chiral. By applying this definition in 2D or 3D, one can distinguish between 2D chirality of a flat spiral, which reverses its twist when observed from opposite sides, and 3D chirality of a helix, which has the same twist when observed from opposite ends. Chiral media can interact differently with circularly polarized waves of opposite handedness. 3D chirality leads to optical activity, which is the same for opposite propagation directions. 2D chirality leads to circular conversion dichroism, a reciprocal effect that manifests itself as different optical properties for circularly polarized waves of the same handedness illuminating front and back of lossy, anisotropic 2D-chiral structures.[5] These directional asymmetries in transmission, reflection and absorption are caused by different left-to-right and right-to-left field conversion

efficiencies. Just like the perceived twist of planar patterns reverses for opposite directions of observation, these conversion efficiencies are interchanged for opposite illumination directions. Similarly, the effect is also reversed when the chirality of the pattern is reversed. Strong circular conversion dichroism occurs in arrays of 2D-chiral split rings, which consist of two conductive arcs of different length separated by gaps of different size.[8] For such a split ring, a twist vector *V* may be defined by a corkscrew law as rotation from the short gap via the short arc to the long gap. It follows that the handedness would be reversed if the shorter arc could be extended to become the longer arc. **Figure 2** proposes a 2D-chiral split ring structure with switchable chirality. The structure consists of concentric gold and VO_2 split rings of opposite handedness. Here, the temperature-activated dielectric-to-metal phase transition of VO_2 extends the shorter arc of the conductive structure, making it the longer one upon heating, resulting in handedness reversal and thus switchable circular conversion dichroism. (For completeness, we note that the stack of 2D-chiral gold and VO_2 split rings, or indeed any 2D-chiral structure on a substrate, results in a geometry that also has 3D chirality.[51] This is negligible in our case. The split ring stack can still be considered planar as it is about 1000× thinner than the wavelength, and we do not observe any evidence of 3D chirality in the structure's electromagnetic response, see below.)

The spectral response of all proposed structures has been optimized using CST MICROWAVE STUDIO™ by modelling normal incidence of a plane wave onto a single unit cell with periodic boundaries in the lateral directions. The different materials are described by a conductivity 3.56×10^7 S/m for gold, dielectric constant 9.67 for sapphire, dielectric constant 2.93 and loss tangent delta 0.044 for polyimide (used in later sections).

VO_2 was modeled with different conductivities ranging from 10 S/m for the low-temperature dielectric state to 2.6×10^5 S/m for the high-temperature metallic state.[47] (For measurements of morphology and temperature-dependent conductivity at THz frequencies of the fabricated VO_2 film see Supplementary **Figures S1** and **S2**.).

Figure 3 shows the spectral dependence of the metamaterial's transmission and reflection characteristics for RCP (+) and LCP (-) THz waves when VO_2 is in its insulator (left) or metallic (right) phase according to our simulations. For example, the fractions of incident RCP intensity that are transmitted as RCP and LCP are given by $|T_{++}|^2$ and $|T_{-+}|^2$, respectively. Here RCP corresponds to clockwise rotation of the electric field vector at a fixed position as seen by an observer looking from within the beam towards the source. Direct transmission is identical for both circular polarizations, $|T_{++}|^2 = |T_{--}|^2$, indicating the absence of optical activity (Figure 3a and 3b). However, significant resonant circular conversion dichroism, $|T_{-+}|^2 \neq |T_{+-}|^2$, is observed. At low VO_2 conductivity, preferential transmission of incident LCP is observed at the 0.64 THz resonance (Figure 3a), whereas at high VO_2 conductivity incident RCP is transmitted preferentially at the resonance that red-shifts to 0.56 THz (Figure 3b) due to a slightly larger electrical length of the VO_2 split rings compared to the gold ones. The observed conversion dichroism can be quantified as $\Delta T_+ = |T_{-+}|^2 - |T_{+-}|^2$, which equals the difference in total transmission for RCP and LCP incident on the sapphire side of the sample as optical activity is absent in our case. ΔT_+ is known as transmission asymmetry as it corresponds to the difference in total transmission for RCP incident on the sapphire and gold sides (front and back) of the metamaterial.[5] The corresponding asymmetry for incident LCP is given by $\Delta T_- = -\Delta T_+$. Importantly, the

resonant transmission asymmetry changes sign from -10% to +5% upon heating-induced switching of VO_2 from dielectric to metal (Figure 3c and 3d). Thus, our simulations demonstrate heating-induced handedness reversal of 2D chirality and switchable circular conversion dichroism.

Switchable circular conversion dichroism is also observed in reflection. When assessing the handedness of reflected waves, we need to take into account that incident and reflected waves propagate in opposite directions and therefore their handedness is determined by observers that look in opposite directions. Thus, co-rotating incident and reflected fields, that result from normal reflection of a circularly polarized wave (e.g. by a metallic mirror), have opposite handedness. Therefore, $|R_{-+}|^2$ corresponds to direct reflection of incident RCP, while the reflection asymmetry due to circular conversion dichroism is given by $\Delta R_+ = |R_{++}|^2 - |R_{--}|^2$. We observe identical direct reflection of RCP and LCP, $|R_{-+}|^2 = |R_{+-}|^2$ (Figure 3e and 3f) and resonant circular conversion dichroism $|R_{++}|^2 \neq |R_{--}|^2$ (Figure 3e and 3f). The latter occurs at the same resonances as for transmission, but reaches larger values of $\Delta R_+ = -23\%$ and $+12\%$ for the dielectric and metallic phases of VO_2, respectively (Figure 3g and 3h).

For completeness, we note that differences between $|R_{-+}|^2$and $|R_{+-}|^2$ could result from the Faraday effect in combination with a conventional handedness-reversing reflection or from optical activity (circular dichroism) in combination with a handedness-preserving reflection. Throughout all results reported in this paper, $|R_{-+}|^2 = |R_{+-}|^2$ within numerical and experimental accuracy.

The observed switchable circular conversion dichroism may be understood in terms of the

resonant current distributions that incident LCP and RCP excite in the split rings. These are revealed by the magnetic field perpendicular to the metamaterial plane, which arises from currents within the metamaterial structure according to Ampère's Law. Our simulations reveal two types of current distributions, electric and magnetic dipole modes, d and m (**Figure 4**). Linear electric dipole modes are dominated by currents in one direction (at a moment in time, see white arrows). They radiate efficiently, causing substantial circular conversion generating a field that counter-rotates compared to that of the incident circularly polarized wave. In contrast, magnetic dipole modes are dominated by anti-symmetric charge oscillations in opposite sections of the ring, which lead to a magnetic moment perpendicular to the metamaterial plane. Magnetic dipole modes trap energy at the metamaterial surface, which is eventually dissipated in the lossy polyimide, resulting absorption instead of circular conversion.[52] At the resonance, in case of low VO_2 conductivity, LCP incident on the substrate side of our metamaterial excites a linear electric dipole mode (Figure 4a) that yields large circular conversion ($|T_{+-}|^2$ and $|R_{--}|^2$ in Figure 3a and 3e) while RCP excites a magnetic dipole mode (Figure 4c) with negligible circular conversion ($|T_{-+}|^2$ and $|R_{++}|^2$ in Figure 3a and 3e). When the dielectric-to-metal phase transition of VO_2 reverses the handedness of the split rings, by turning the shorter conductive arc into the longer one, LCP and RCP excite the opposite type of mode (Figure 4b and 4d), respectively, resulting in reversed circular conversion dichroism (Figure 3b and 3f).

2.2 Switchable Chiral Mirrors

For a single illuminating wave, theoretical derivation indicates that absorption in a planar metasurface (without substrate) cannot exceed 50%, limiting the absorption, transmission,

and reflection asymmetries to 50%, 25%, and 25%, respectively.[53] However, in-phase coherent illumination by counterpropagating waves can yield "coherent perfect absorption" by a planar metasurface.[54] Inspired by this strategy, we construct three LCP mirrors by introducing a backing conventional mirror as shown below. In this situation, the incident wave and (multiple) reflection(s) by the conventional mirror lead to coherent illumination of "front" and "back" of the 2D-chiral metasurface, which can yield coherent perfect absorption in case of constructive interference on the metasurface.[2] We space a 2D-chiral metasurface and a mirror by lossy polyimide with a thickness that is chosen to achieve in-phase metasurface excitation and thus absorption of one resonant circular polarization.[15] Here, different types of VO_2 rings have been inserted between chiral gold split rings and the sapphire substrate, in order to control the anisotropy and chirality of the structure upon heating of VO_2 to its metallic phase, resulting in different types of switchable chiral mirrors. All switchable chiral mirrors were fabricated by defining a 150-nm-thick VO_2 ring structure on a 500-µm-thick c-cut sapphire substrate using optical lithography and plasma etching (CF_4/O_2). A second lithography step was performed to define the 200-nm-thick gold chiral split rings on top of the VO_2/sapphire sample using gold deposition and a lift-off step. Then, polyimide of appropriate thickness was coated on the top of each sample. Finally, a 200-nm-thick gold layer was deposited on the polyimide layer to act as a mirror. The spectral dependence of reflectivity of the fabricated structures was measured at normal incidence using THz time-domain spectroscopy. The temperature of the metamaterial was controlled using a hot plate with a hole for THz wave transmission and the actual sample temperature was measured with a thermometer. The insulator-to-metal phase transition of VO_2 occurs at

65-75 °C. In order to characterize our samples for both phases of VO_2, we controlled the sample temperature from a much lower temperature (room temperature, 23 °C), where VO_2 can be assumed to be insulating, to a much higher temperature (91-108 °C), where VO_2 can be assumed to be metallic.

2.2.1. Switching between Chiral Mirror and Conventional Mirror

A conventional mirror is isotropic, while a chiral mirror is inherently anisotropic. Therefore, a mirror design that allows switching of a chiral mirror into a conventional mirror must eliminate the structure's anisotropy upon switching. This would be achieved by transforming the metallic chiral split rings into continuous conductive rings, which are achiral and isotropic. To achieve this, we propose the unit cell design of **Figure 5**, which places a chiral split gold ring directly on a continuous VO_2 ring, exploiting the phase transition of VO_2 to close the gaps of the conductive ring structure upon heating. Dimensions that are specific to this chiral mirror are given in Figure 5 and its caption, while information relevant to the structure of all chiral mirrors and their fabrication is given in section 2.2.

Figure 6 shows the spectral dependence of the switchable mirror's reflectivity according to simulations (top) and measurements (bottom) when VO_2 is in its room-temperature insulating phase (left) or its high-temperature conductive phase (right). At room temperature, the structure is an LCP mirror at its resonance (0.65 THz in Figure 6a, 0.71 THz in Figure 6c). Here, LCP intensity is almost fully reflected without handedness change ($|R_{--}|^2$), while all other components of reflectivity are small. Incident RCP is almost fully absorbed. This corresponds to near-perfect circular conversion dichroism with ΔR_- of almost unity. Away from its resonance frequency, the structure is a handedness-preserving mirror ($|R_{++}|^2 \approx$

$|R_{--}|^2$ close to unity). Upon heating, the insulator-to-metal transition of VO_2 transforms the split rings into continuous conductive rings. As a result, the resonance and circular conversion dichroism vanish, and the structure becomes a conventional mirror which reverses the handedness of incident circular polarization upon reflection ($|R_{-+}|^2 = |R_{+-}|^2$ dominate, Figure 6b and 6d). Here, the phase transition of VO_2 switches circular conversion dichroism on/off. Thus, our results demonstrate switching of an LCP mirror into a conventional mirror (at resonance) and switching of a handedness-preserving mirror into a conventional mirror (off-resonance).

Regarding the high-temperature state of the mirror, we note that $|R_{++}|^2$ and $|R_{--}|^2$ would vanish completely for a perfectly isotropic structure (e.g. perfect rings). Here, these values remain non-zero due to residual anisotropy arising from the presence of the gold split rings. Thicker VO_2 and/or use of a continuous VO_2 layer rather than rings may result in more ideal conventional mirror properties at high temperatures.

Both here and in subsequent sections, experimental results and simulations are in qualitative agreement. A 0.06 THz blue-shift of the resonance's spectral position and reduced contrast in the experiments are related to fabrication accuracy of the metamaterial, polyimide thickness, limited accuracy of material parameters and limited spectral resolution of the THz time domain spectroscopy setup.

The physical mechanism behind the heating-induced switching from LCP mirror to conventional mirror is revealed by our simulations, which show how incident LCP and RCP interact with the metamaterial layer at 0.65 THz (**Figure 7**). The resonant LCP mirror response at low VO_2 conductivity results from excitation of a linear electric dipole mode by

LCP (Figure 7a) and a magnetic dipole mode by RCP (Figure 7c), causing large circular conversion and large absorption, respectively, as discussed in section 2.1. It is interesting to note why the electric dipole mode can cause near-perfect reflection of LCP as LCP. An ideal linear electric dipole will radiate linear polarization, i.e. a superposition of equally-strong fields of opposite handedness. Field radiated along $-z$ and $+z$ that co-rotates with the incident field can (destructively) interfere with the incident field (along $-z$) and its reflection by a conventional mirror (along $+z$), allowing it to vanish in an optimized structure. Radiated fields that counter-rotate compared to the incident field remain (circular conversion). These counter-rotating incident and reflected fields have the same circular polarization as they counter-propagate, implying that their handedness must be assessed by observers that look in opposite directions.

When the conductive split rings are transformed into isotropic continuous rings by the heating-induced dielectric-to-metal phase transition of VO_2, the metamaterial response becomes isotropic, as it should for normal incidence onto a conventional mirror. The currents reveal circular electric dipole excitations that simply follow the orientation of the incident circularly polarized wave's rotating electric field (Figure 7b and 7d). Incident fields, dipoles and radiated fields all co-rotate, as for any conventional mirror. The corresponding incident and reflected waves have circular polarizations of opposite handedness as the reversal of the propagation direction upon reflection means that the handedness of incident and reflected waves is assessed by observers looking in opposite directions.

2.2.2. Switching between LCP Mirror and Handedness-preserving Mirror

A handedness-preserving mirror exhibits the same anisotropic response for illumination

with circularly polarized waves of either handedness, while the function of a chiral mirror relies on different responses to RCP and LCP illumination. Therefore, the transformation of a chiral mirror into a handedness-preserving mirror requires elimination of the structure's chiral response, while retaining its anisotropy. This would be achieved by transforming the metallic chiral split rings into achiral split rings consisting of equal conductive arcs separated by equal gaps. In order to realize a transformation into such an achiral anisotropic structure, we propose the unit cell design of **Figure 8**, which places a chiral split gold ring directly on an achiral split VO_2 ring, exploiting the phase transition of VO_2 to eliminate the differences between the arcs and gaps of the conductive ring structure upon heating. See Figure 8 and its caption for mirror-specific dimensions and section 2.2 for details relevant to structure and fabrication of all chiral mirrors.

Figure 9 shows the spectral dependence of the switchable mirror's reflectivity according to simulations (top) and measurements (bottom) when VO_2 is in its room-temperature insulating phase (left) or its high-temperature conductive phase (right). At room temperature, the structure is an LCP mirror with approximately the same properties as the chiral mirror discussed in the previous section. At its resonance, LCP intensity is almost fully reflected without handedness change ($|R_{--}|^2$), while RCP is almost fully absorbed (Figures 9a and 9c). Away from its chiral resonance, the structure is a handedness-preserving mirror that reflects both circular polarizations with high efficiency. Upon heating, the insulator-to-metal transition of VO_2 transforms the chiral split rings into achiral split rings. As a result, the chiral resonance vanishes, and the structure becomes a handedness-preserving mirror throughout the studied spectral range ($|R_{++}|^2 \approx |R_{--}|^2$ dominate, $|R_{+-}|^2 \approx |R_{-+}|^2$ remain

negligible, Figures 9b and 9d). Thus, our results demonstrate on/off switching of circular conversion dichroism and switching of an LCP mirror into a handedness-preserving mirror.

Regarding the high-temperature state of the mirror, we note that $|R_{++}|^2$ and $|R_{--}|^2$ would be exactly identical for a perfectly achiral structure. Here, a small difference remains due to residual chirality arising from the presence of the chiral gold split rings. Thicker VO_2 may result in more perfect handedness-preserving mirror properties with further reduced circular conversion dichroism at high temperatures.

The physical origin of the heating-induced switching from LCP mirror to handedness-preserving mirror is revealed by our simulations, which show how incident LCP and RCP interact with the metamaterial layer at 0.65 THz (**Figure 10**). The resonant LCP mirror response at low VO_2 conductivity is caused by an LCP-induced electric dipole excitation (Figure 10a) that causes near-complete circular conversion ($|R_{--}|^2$) and an RCP-induced magnetic dipole excitation (Figure 10b) that causes near-complete absorption, in the same way as discussed for the previous structure. When the conductive chiral split rings are transformed into achiral split rings by the heating-induced dielectric-to-metal phase transition of VO_2, the metamaterial response becomes (approximately) achiral. The currents reveal electric dipoles that oscillate (approximately) along the vertical symmetry axis of the split rings regardless of the handedness of the incident circularly polarized wave (Figures 10b and 10d). These linear electric dipoles cause near-complete circular conversion ($|R_{--}|^2$ and $|R_{++}|^2$, respectively) in the same way as for Figure 10a.

2.2.3. Switching between LCP Mirror and RCP Mirror

Chiral mirrors of opposite handedness require structures with opposite circular conversion

dichroism. Therefore, the transformation of a chiral mirror into one of opposite handedness requires reversal of the handedness of the metasurface layer, as in section 2.1. In order to realize a transformation of a chiral mirror into one of opposite handedness, we propose the unit cell design of **Figure 11**, which places a chiral split gold ring directly on a chiral split VO_2 ring of opposite handedness. This design exploits the phase transition of VO_2 to extend the shorter arc of the gold structure to become the longer conductive arm, reversing the handedness of the conductive structure upon heating. The twist defined as rotation from the short gap via the short arc to the long gap is clockwise for the gold split ring and anti-clockwise for the VO_2 split ring, corresponding to twist vectors pointing away from the reader ($\vec{V}_{Au}$) and towards the reader ($\vec{V}_{VO_2}$), respectively. See Figure 11 and its caption for mirror-specific dimensions and section 2.2 for details relevant to structure and fabrication of all chiral mirrors.

Figure 12 shows the spectral dependence of the switchable mirror's simulated (top) and measured (bottom) reflectivity when VO_2 is in its room-temperature insulating phase (left) or its high-temperature conductive phase (right). At room temperature, the structure is an LCP mirror with approximately the same properties as the chiral mirrors discussed above. At its resonance, LCP intensity is almost fully reflected without handedness change ($|R_{--}|^2$), while RCP is almost fully absorbed (Figures 12a and 12c). Away from its chiral resonance and above 0.5 THz, the structure is a handedness-preserving mirror that reflects both circular polarizations with high efficiency. Upon heating, the insulator-to-metal transition of VO_2 reverses the handedness of the conductive chiral split rings. As a result, structure transforms into an RCP mirror that reflects incident RCP without handedness change while (mostly)

absorbing LCP at its chiral resonance (Figures 12b and 12d). The chiral resonance red-shifts due to a slightly increased electrical length of the VO_2 split rings compared to the gold split rings. The observed difference in absolute reflectivity at the chiral resonance switches from $\Delta R_+ \approx -75\%$ to about +55%. Our results demonstrate switching of an LCP mirror into an RCP mirror.

The physical origin of the heating-induced switching between LCP mirror and RCP mirror is revealed by simulations of the modes excited by incident LCP and RCP at the structure's chiral resonance (**Figure 13**). The resonant LCP mirror response at low VO_2 conductivity is caused by an LCP-induced electric dipole excitation (Figure 13a) that causes near-complete circular conversion ($|R_{--}|^2$) and an RCP-induced magnetic dipole excitation (Figure 13b) that causes near-complete absorption, in the same way as for the previous structures. When the handedness of the conductive chiral split rings is reversed by the heating-induced dielectric-to-metal phase transition of VO_2, the modes excited by LCP and RCP interchange (Figures 13b and 13d), causing handedness-preserving reflection and absorption of the opposite circular polarizations.

3. Conclusion

In summary, we have demonstrated switching of chirality and anisotropy of planar structures. Exploiting the temperature-controlled dielectric-to-metal phase transition of VO_2 to reverse or eliminate the 2D chirality of metasurfaces, we have demonstrated both handedness switching and on/off switching of circular conversion dichroism. We have exploited these effects to realize switchable chiral mirrors. Upon heating, these LCP mirrors become either a conventional mirror, a handedness-preserving mirror or an RCP mirror for THz waves. We

note that switching between a handedness-preserving and a conventional (handedness reversing) mirror function was also observed. These functionalities have been traced to excitation of different current modes by incident LCP and RCP, where magnetic dipole modes are responsible for absorption, linear electric dipole modes cause handedness-preserving reflection (circular conversion) and circular electric dipole modes cause handedness-reversing reflection. Switchable chiral mirrors can be applied for active control over reflection, absorption and polarization of light, e.g. to realize cavities and lasers that can be switched between differently polarized modes.

Supporting Information

Supporting Information is available from the Wiley Online Library or from the author. The data from this paper is available from the University of Southampton ePrints research repository: https://doi.org/10.5258/SOTON/D1230

Acknowledgements

This work was supported by the National Key Research and Development Program of China (with grant NO. 2017YFA0701004), the National Science Foundation of China (Grant Nos. 61935015, 61875150, 61735012 and 61871212), the Tianjin Municipal Fund for Distinguished Young Scholars (18JCJQJC45600) and the UK's Engineering and Physical Sciences Research Council (grant EP/M009122/1).

Conflict of Interest

The authors declare no conflict of interest.

Author Contributions

M. Liu and E. Plum contributed equally to this work. M. Liu. conducted the experiments and simulations. M. Liu., H. Li, S.-Y. Duan, C.-H. Zhang, C.-W. Zou and B.-B. Jin fabricated the metamaterial structures. S.-X. Li constructed the reflective terahertz time-domain spectroscopy setup. M. Liu, E. Plum, Q. Xu., X.-Q. Zhang, J.-G. Han and W.-L. Zhang interpreted the results. M. Liu and E. Plum wrote the manuscript. E. Plum, J.-G. Han and W.-L. Zhang supervised the project. E. Plum proposed the project.

References

[1] M. Martinelli, *Opt. Commun.* **1989**, *72*, 341-344.

[2] E. Plum, N. I. Zheludev, *Appl. Phys. Lett.* **2015**, *106*, 221901.

[3] V. A. Fedotov, P. L. Mladyonov, S. L. Prosvirnin, N. I. Zheludev, *Phys. Rev. E* **2005**, *72*, 056613.

[4] V. A. Fedotov, A. V. Rogacheva, N. I. Zheludev, P. L. Mladyonov, S. L. Prosvirnin, *Appl. Phys. Lett.* **2006**, *88*, 091119.

[5] V. A. Fedotov, P. L. Mladyonov, S. L. Prosvirnin, A. V. Rogacheva, Y. Chen, N. I. Zheludev, *Phys. Rev. Lett.* **2006**, *97*, 167401.

[6] V. A. Fedotov, A. S. Schwanecke, N. I. Zheludev, V. V. Khardikov, S. L. Prosvirnin, *Nano Lett.* **2007**, *7*, 1996-1999.

[7] A. Drezet, C. Genet, J. Y. Laluet, T. W. Ebbesen, *Opt. Express* **2008**, *16*, 12559-12570.

[8] E. Plum, V. A. Fedotov, N. I. Zheludev, *Appl. Phys. Lett.* **2009**, *94*, 131901.

[9] S. V. Zhukovsky, A. V. Novitsky, V. M. Galynsky, *Opt. Lett.* **2009**, *34*, 1988-1990.

[10] E. Plum, V. A. Fedotov, N. I. Zheludev, *J. Opt.* **2011**, *13*, 024006.

[11] A. V. Novitsky, V. M. Galynsky, S. V. Zhukovsky, *Phys. Rev. B* **2012**, *86*, 075138.

[12] Z. F. Li, M. Gokkavas, E. Ozbay, *Adv. Opt. Mater.* **2013**, *1*, 482-488.

[13] L. Wu, Z. Y. Yang, Y. Z. Cheng, M. Zhao, R. Z Gong, Y. Zheng, J. A Duan, X. H Yuan, *Appl. Phys. Lett.* **2013**, *103*, 021903.

[14] W. Li, Z. J. Coppens, L. V. Besteiro, W. Wang, A. O. Govorov, J. Valentine, *Nat. Commun.* **2015**, *6*, 8379.

[15] Q. Wang, E. Plum, Q. L. Yang, X. Q. Zhang, Q. Xu, Y. H. Xu, J. G. Han, W. L. Zhang,

Light Sci. Appl. **2018**, *7*, 25.

[16] L. Kang, S. P. Rodrigues, M. Taghinejad, S. Lan, K.-T. Lee, Y. Liu, D. H. Werner, A. Urbas, W. Cai, *Nano Lett.* **2017**, *17*, 7102-7109.

[17] L. Kang, C.-Y. Wang, X. Guo, X. Ni, Z. Liu, D. H. Werner, *Nano Lett.* **2020**, *20*, 2047-2055.

[18] Hu Tao, A. C. Strikwerda, K. Fan, W. J. Padilla, X. Zhang, R. D. Averitt, *Phys. Rev. Lett.* **2009**, *103*, 147401.

[19] J. Y. Ou, E. Plum, L. Jiang, N. I. Zheludev, *Nano Lett.* **2011**, *11*, 2142-2144.

[20] W. M. Zhu, A. Q. Liu, X. M. Zhang, D. P. Tsai, T. Bourouina, J. H. Teng, X. H. Zhang, H. C. Guo, H. Tanoto, T. Mei, G. Q. Lo, D. L. Kwong, *Adv. Mater.* **2011**, *23*, 1792-1796.

[21] Y. H. Fu, A. Q. Liu, W. M. Zhu, X. M. Zhang, D. P. Tsai, J. B. Zhang, T. Mei, J. F. Tao, H. C. Guo, X. H. Zhang, J. H. Teng, N. I. Zheludev, G. Q. Lo, D. L. Kwong, *Adv. Funct. Mater.* **2011**, *21*, 3589-3594.

[22] P. Pitchappa, M. Manjappa, C. P. Ho, R. Singh, N. Singh, C. Lee, *Adv. Opt. Mater.* **2016**, *4*, 541-547.

[23] L. Q. Cong, P. Pitchappa, C. K Lee, R. Singh, *Adv. Mater.* **2017**, *29*, 1700733.

[24] D. H. Werner, D. H. Kwon, I. C. Khoo, A. V. Kildishev, V. M. Shalaev, *Opt. Express* **2007**, *15*, 3342-3347.

[25] N. Kanda, K. Konishi, M. K. Gonokami, *Opt. Express* **2009**, *34*, 3000-3002.

[26] H. T. Chen, W. J. Padilla, J. M. O. Zide, A. C. Gossard, A. J. Taylor, R. D. Averitt, *Nature* **2006**, *444*, 597-600.

[27] H. T. Chen, S. Palit, T. Tyler, C. M. Bingham, J. M. O. Zide, J. F. O'Hara, D. R. Smith, A.

C. Gossard, R. D. Averitt, W. J. Padilla, N. M. Jokerst, A. J. Taylor, *Appl. Phys. Lett.* **2008**, *93*, 091117.

[28] T. Driscoll, S. Palit, M. M. Qazilbash, M. Brehm, F. Keilmann, B. G. Chae, S. J. Yun, H. T. Kim, S. Y. Cho, N. M. Jokerst, D. R. Smith, D. N. Basov, *Appl. Phys. Lett.* **2008**, *93*, 024101.

[29] T. Driscoll, H. T. Kim, B. G. Chae, B. J. Kim, Y. W. Lee, N. M. Jokerst, S. Palit, D. R. Smith, M. D. Ventra, D. N. Basov, *Science* **2009**, *325*, 1518-1521.

[30] L. Liu, L. Kang, T. S. Mayer, D. H. Werner, *Nat. Commun.* **2016**, *7*, 13236.

[31] F. Ding, S. M. Zhong, S. I. Bozhevolnyi, *Adv. Opt. Mater.* **2018**, *6*, 1701204.

[32] H. T. Chen, J. F. O'Hara, A. K. Azad, A. J. Taylor, R. D. Averitt, D. B. Shrekenhamer, W, J. Padilla, *Nat. Photonics* **2008**, *2*, 295-298.

[33] J. G. Han, A. Lakhtakia, Z. Tian, X. C. Lu, W. L. Zhang, *Opt. Lett.* **2009**, *34*, 1465-1467.

[34] M. J. Dicken, K. Aydin, I. M. Pryce, L. A. Sweatlock, E. M. Boyd, S. Walavalkar, J. Ma, H. A. Atwater, *Opt. Express* **2009**, *17*, 18330-18339.

[35] W. X. Huang, X. G. Yin, C. P. Huang, Q. J. Wang, T. F. Miao, Y. Y. Zhu, *Appl. Phys. Lett.* **2010**, *96*, 261908.

[36] P. V. Kapitanova, S. I. Maslovski, I. V. Shadrivov, P. M. Voroshilov, D. S. Filonov, P. A. Belov, Y. S. Kivshar, *Appl. Phys. Lett.* **2011**, *99*, 251914.

[37] D. Shrekenhamer, S. Rout, A. C. Strikwerda, C. Bingham, R. D. Averitt, S. Sonkusale, W. J. Padilla, *Opt. Express* **2011**, *19*, 9968-9975.

[38] J. Q. Gu, R. Singh, X. J. Liu, X. Q. Zhang, Y. F. Ma, S. Zhang, S. A. Maier, Z. Tian, A. K. Azad, H. T. Chen, A. J. Taylor, J. G. Han, W. L. Zhang, *Nat. Commun.* **2012**, *3*, 1151.

[39] Y. H. Zhu, S. Vegesna, Y. Zhao, V. Kuryatkov, M. Holtz, Z. Y. Fan, M. Saed, A. A. Bernussi, *Opt. Lett.* **2013**, *38*, 2382-2384.

[40] P. Q. Liu, I. J. Luxmoore, S. A. Mikhailov, N. A. Savostianova, F. Valmorra, J. Faist, G. R. Nash, *Nat. Commun.* **2015**, *6*, 8969.

[41] Q. Xu, X. Q. Su, C. M. Ouyang, N. N. Xu, W. Cao, Y. P. Zhang, Q. Li, C. Hu, J. Q. Gu, Z. Tian, A. K. Azad, J. G. Han, W. L. Zhang, *Opt. Lett.* **2016**, *41*, 4562-4565.

[42] H. L. Cai, S. Chen, C. W. Zou, Q. P. Huang, Y. Liu, X. Hu, Z. P. Fu, Y. Zhao, H. C. He, Y. L. Lu, *Adv. Opt. Mater.* **2018**, *6*, 1800257.

[43] M. Liu, Q. Xu, X. Y. Chen, E. Plum, H. Li, X. Q. Zhang, C. H. Zhang, C. W. Zou, J. G. Han, W. L. Zhang, *Sci. Rep* **2019**, *9*, 4097.

[44] J. G. Han, A. Lakhtakia, C. W. Qiu, *Opt. Express* **2008**, *16*, 14390-14396.

[45] H. Nemec, P. Kuzel, F. Kadlec, C. Kadlec, R. Yahiaoui, P. Mounaix, *Phys. Rev. B* **2009**, *79*, 241108.

[46] J. G. Han, A. Lakhtakia, *J. Mod. Opt.* **2009**, *56*, 554-557.

[47] Q. Y. Wen, H. W. Zhang, Q. H. Yang, Y. S. Xie, K. Chen, Y. L. Liu, *Appl. Phys. Lett.* **2010**, *97*, 021111.

[48] M. K. Liu, H. Y. Hwang, H. Tao, A. C. Strikwerda, K. B. Fan, G. R. Keiser, A. J. Sternbach, K. G. West, S. Kittiwatanakul, J. W. Lu, S. A. Wolf, F. G. Omenetto, X. Zhang, K. A. Nelson, R. D. Averitt, *Nature* **2012**, *487*, 345-348.

[49] Y. H. Zhu, Y. Zhao, M. Holtz, Z. Y. Fan, A. A. Bernussi1, *J. Opt. Soc. Am. B* **2012**, *29*, 2373-2378.

[50] O. L. Muskens, L. Bergamini, Y. Wang, J. M. Gaskell, N. Zabala, CH de Groot, D. W.

Sheel, J. Aizpurua, *Light Sci. Appl.* **2016**, *5*, e16173.

[51] M. Kuwata-Gonokami, N. Saito, Y. Ino, M. Kauranen, K. Jefimovs, T. Vallius, J. Turunen, Y. Svirko, *Phys. Rev. Lett.* **2005**, *95*, 227401.

[52] V. A. Fedotov, M. Rose, S. L. Prosvirnin, N. Papasimakis, N. I. Zheludev, *Phys. Rev. Lett.* **2007**, *99*, 147401.

[53] Eric Plum, *Chirality and Metamaterials*, University of Southampton, February, **2010**.

[54] J. F. Zhang, K. F. MacDonald, N. I. Zheludev, *Light-Sci. Appl.* **2012**, *1*, e18.

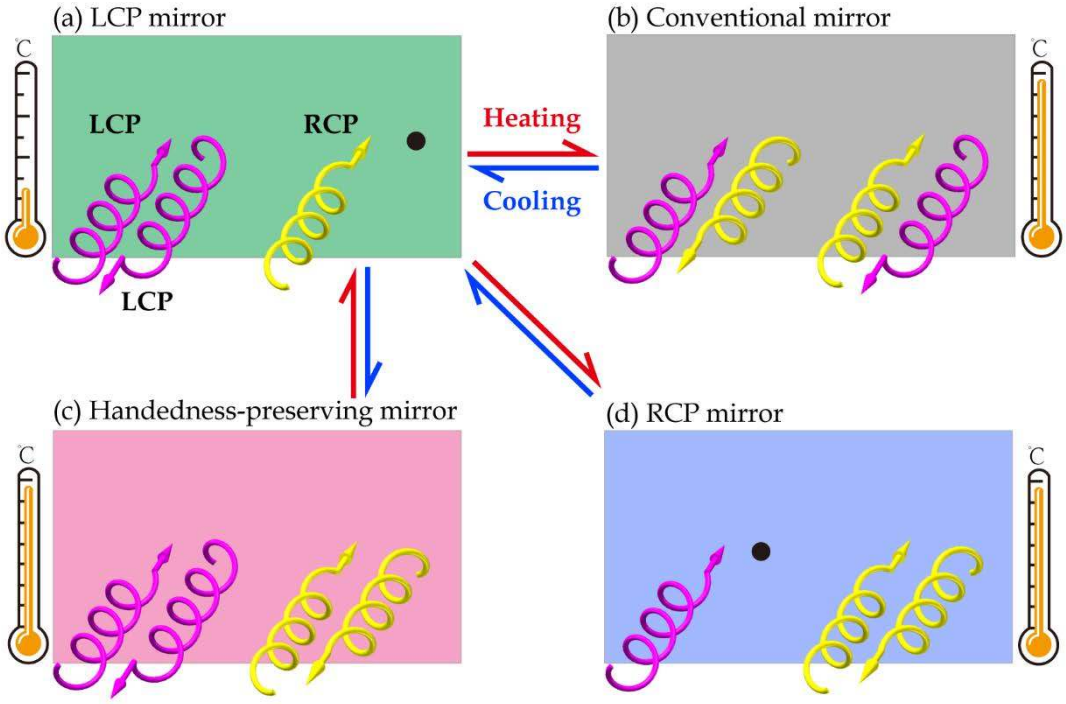

Figure 1. Switchable chiral mirrors. We report (a) room temperature LCP mirrors that transform upon heating into either (b) a conventional mirror, (c) a handedness-preserving mirror or (d) an RCP mirror. A LCP/RCP mirror reflects LCP/RCP without handedness change, while absorbing the other circular polarization. In contrast, conventional/handedness-preserving mirrors reflect both circular polarizations with/without handedness change.

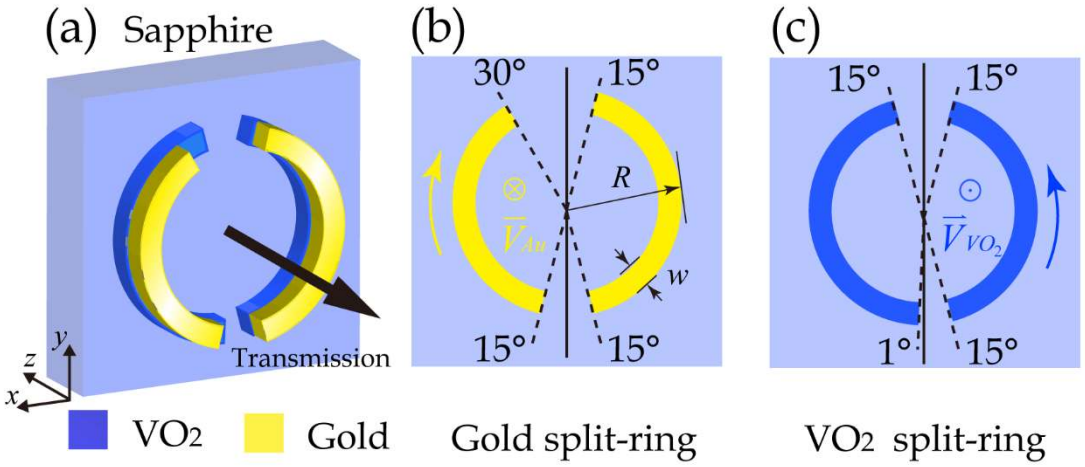

Figure 2. 2D-chiral unit cell of a metamaterial exhibiting switchable circular conversion dichroism. (a) Hybrid unit cell consisting of overlapping concentric (b) 200-nm-thick gold and (c) 150-nm-thick VO_2 asymmetric split rings on a 500-μm-thick c-cut sapphire substrate, with a period of P = 86 μm, ring radius of R = 40 μm and line width of w = 8 μm. The gap sizes and arc lengths differ as shown such that the shorter gold arc is left and the shorter VO_2 arc is right. "Twist vectors" $\vec{V}_{Au}$ and $\vec{V}_{VO_2}$ point away from and towards the reader, respectively, indicating clockwise and anti-clockwise twist defined by a corkscrew law as rotation from the small to the large gap along the short arc. The large black arrow indicates the illumination direction.

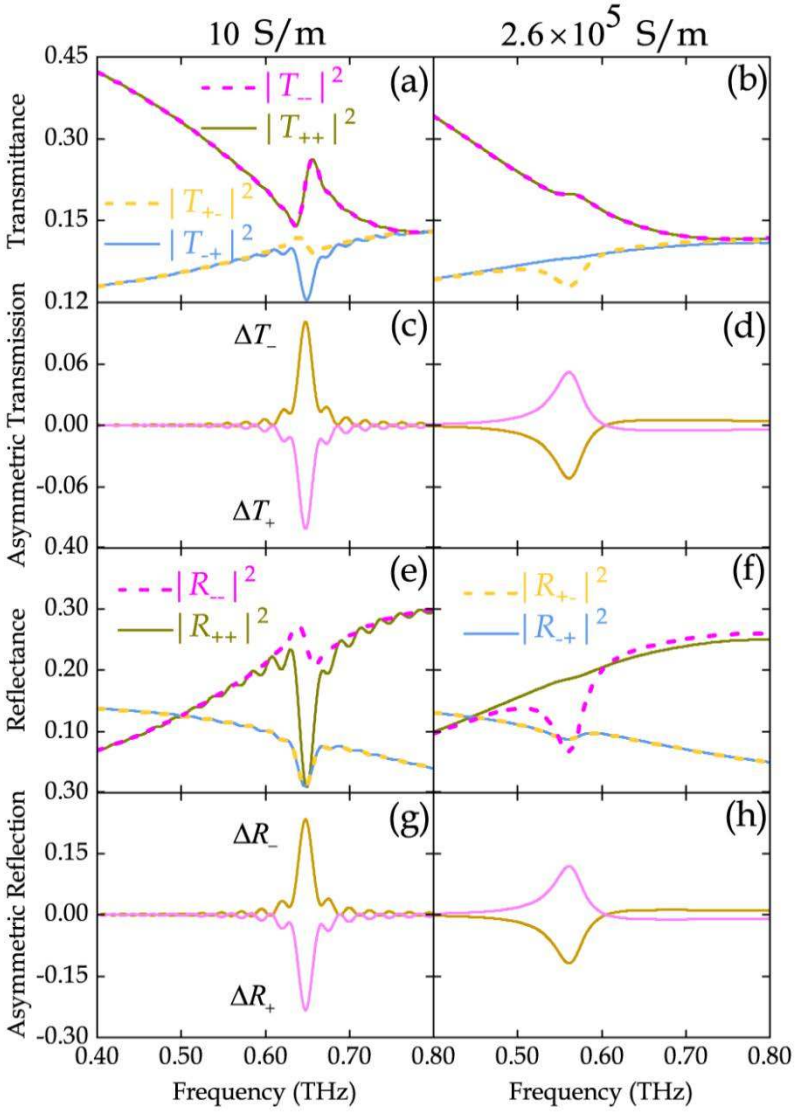

Figure 3. Switching circular conversion dichroism by switching VO_2 between its room-temperature insulator phase (left) and its high-temperature conductive phase (right), corresponding to conductivities σ_{VO_2} of 10 S/m and 2.6×10^5 S/m, respectively, for the metamaterial of Figure 2. Frequency-dependence of (a, b) transmittance, (c, d) transmission asymmetry $\Delta T_+ = |T_{-+}|^2 - |T_{+-}|^2 = -\Delta T_-$, (e, f) reflectance and (g, h) reflection asymmetry $\Delta R_+ = |R_{++}|^2 - |R_{--}|^2 = -\Delta R_-$ in terms of intensity of right-handed (+) and left-handed (-) circularly polarized waves illuminating the split rings from the sapphire side. (The spectral evolution with increasing conductivity of VO_2 is shown in Supplementary **Figures S3-S6**.)

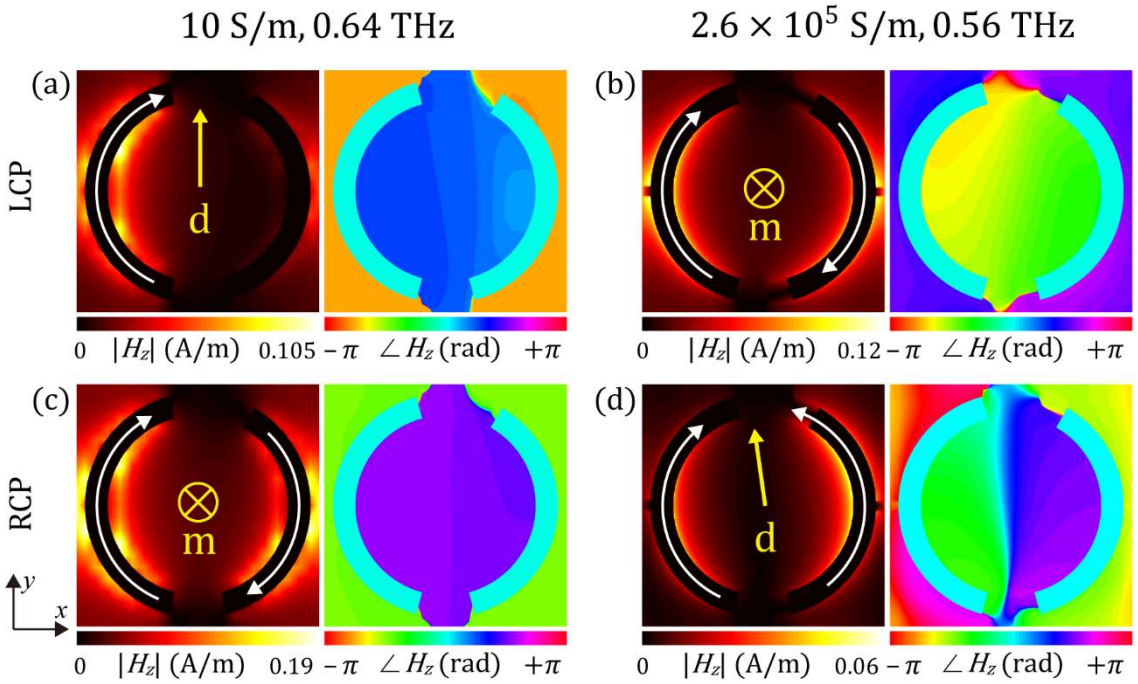

Figure 4. Physical mechanism of switchable circular conversion dichroism of the hybrid 2D-chiral metasurface of Figure 2. Modes excited by (a, b) LCP and (c, d) RCP incident on the substrate-side of the metamaterial for different phases of VO_2. (a, c) 0.64 THz resonance when VO_2 is in its insulating room-temperature phase with $\sigma_{VO_2} = 10$ S/m. (b, d) 0.56 THz resonance when VO_2 is in its conductive high-temperature phase with $\sigma_{VO_2} = 2.6 \times 10^5$ S/m. Amplitude and phase of the magnetic field H_z is shown within the metamaterial plane. The instantaneous directions of currents are marked by white arrows. The resonant currents excited by circular polarizations of opposite handedness correspond to electric and magnetic dipoles, d and m, which interchange upon phase transition of VO_2.

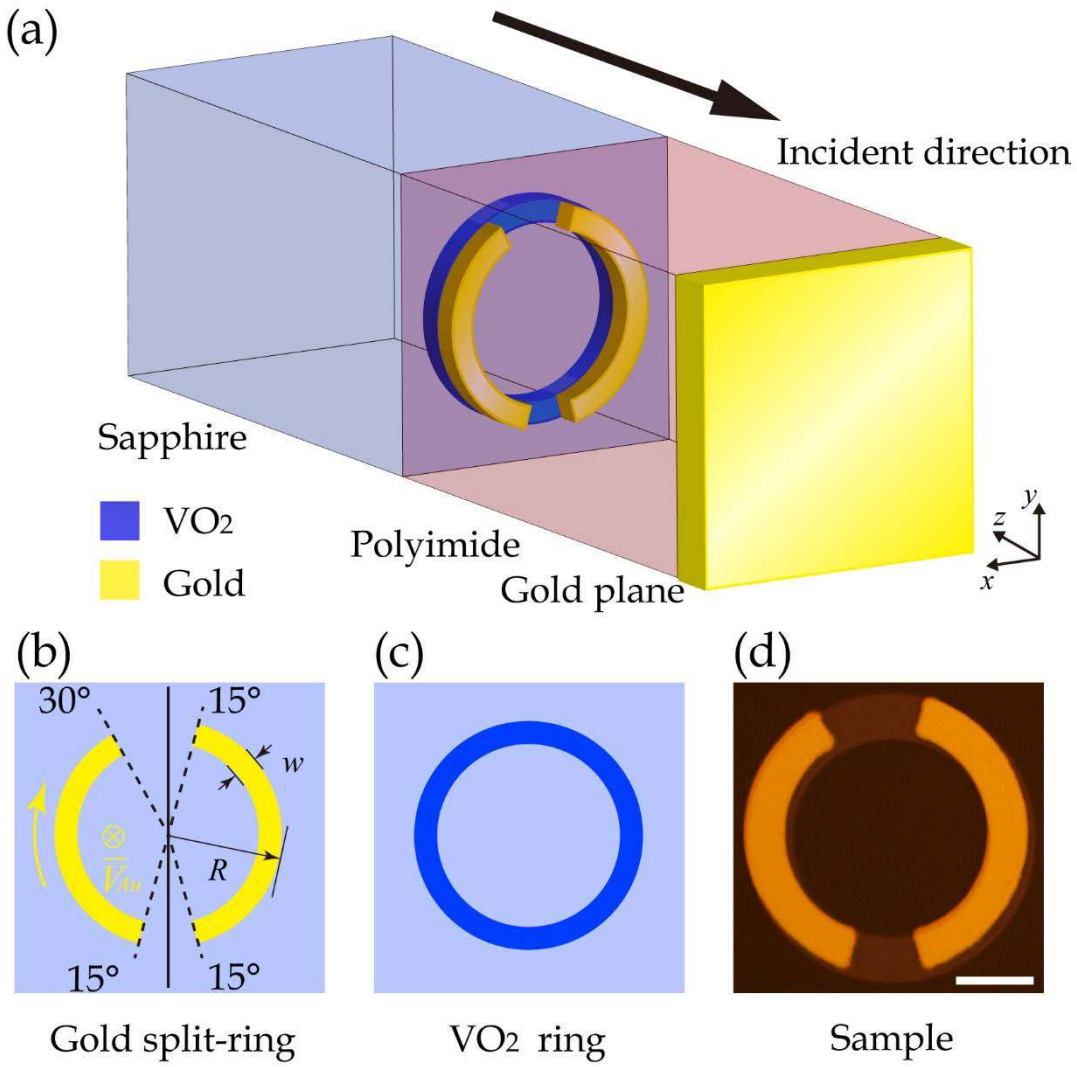

Figure 5. Switchable LCP/conventional mirror. (a) The unit cell consists of a (b) asymmetrically split gold ring and a (c) continuous VO_2 ring, which are concentric and overlap on a sapphire substrate, with a period of P = 80 μm, ring radius of R = 37 μm and line width of w = 11 μm. The "twist vector" $\vec{V}_{Au}$ points away from the reader. A 31-μm-thick polyimide layer separates the sapphire substrate from a gold mirror. (d) Optical microscope image of a unit cell of the fabricated sample observed from the ring structure's gold side with a 20 μm scale bar.

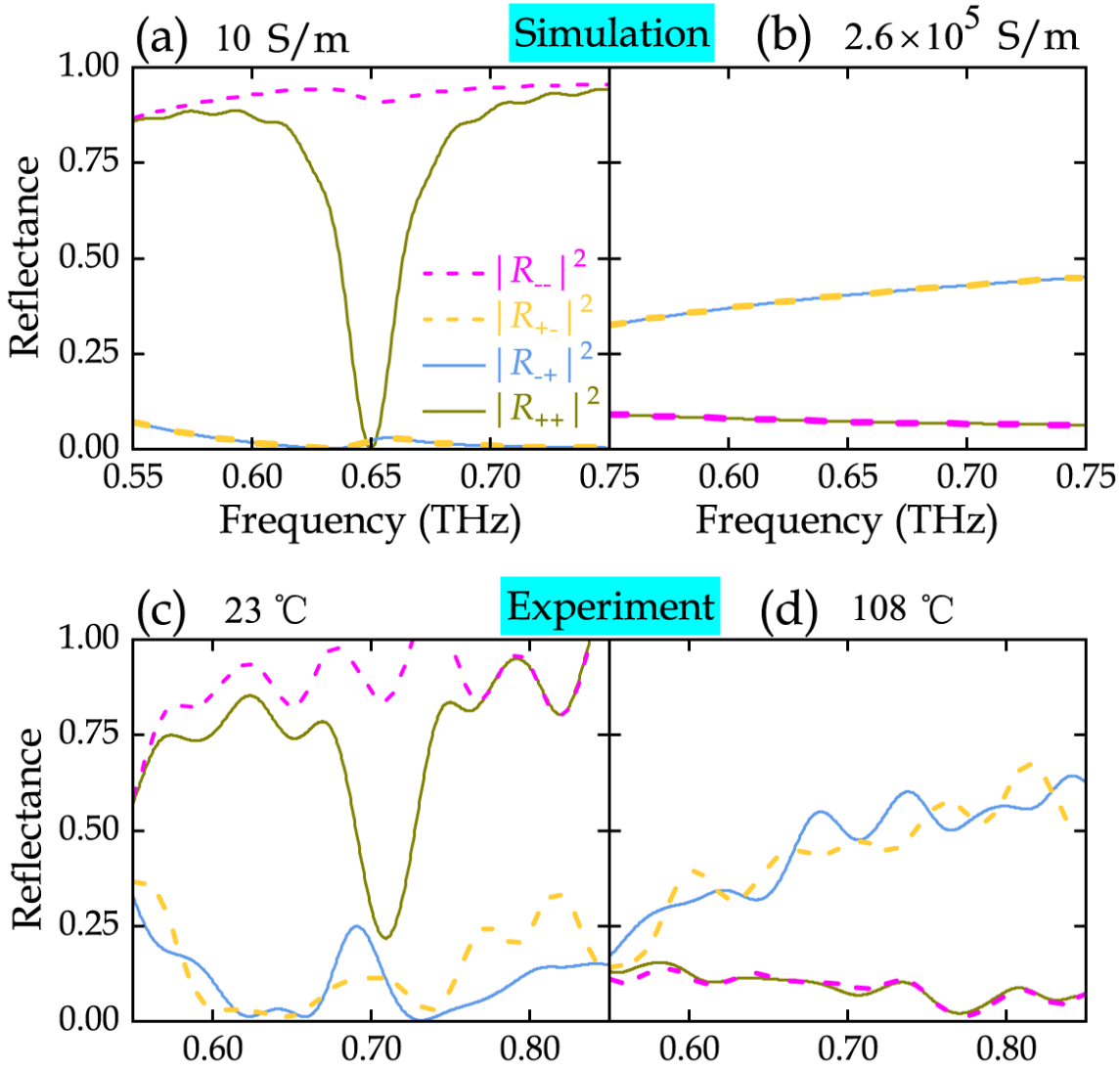

Figure 6. Switching between LCP mirror and conventional mirror based on the transition between the insulator (left) and metal (right) phases of VO_2 for the metamaterial of Figure 5. Reflectance spectra in terms of circular polarization components simulated for VO_2 conductivities of (a) 10 S/m and (b) 2.6×10^5 S/m and corresponding measurements at temperatures of (c) 23 ℃ and (d) 108 ℃. (The spectral evolution with increasing conductivity of VO_2 is shown in Supplementary **Figures S7** and **S8**.)

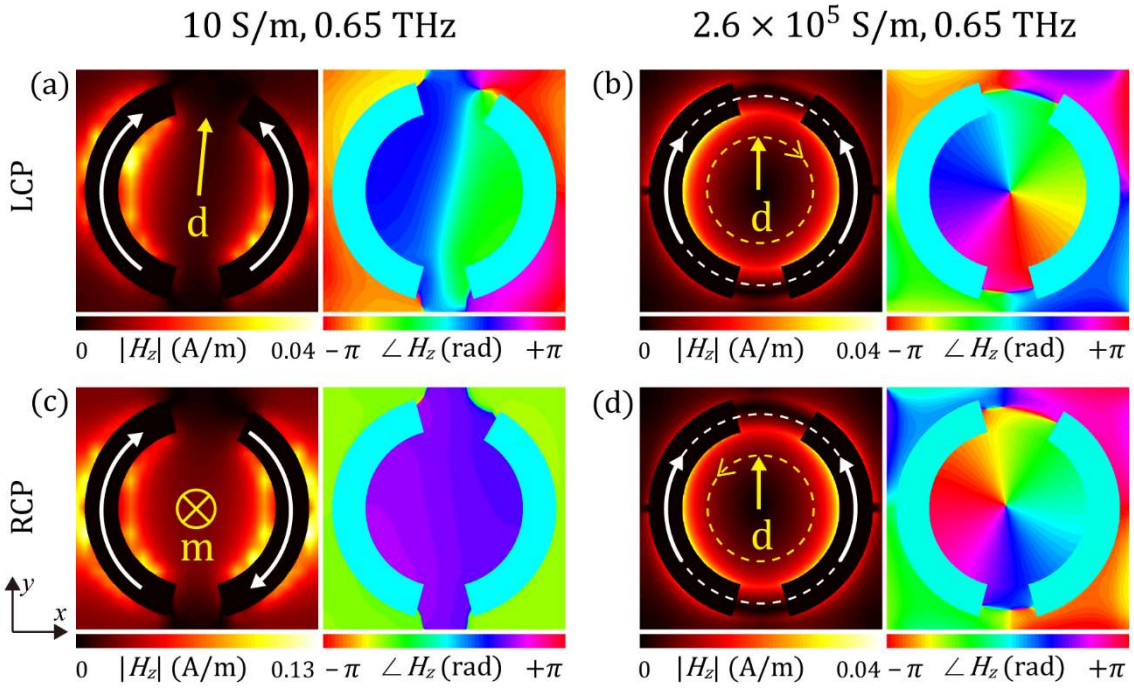

Figure 7. Physical mechanism of LCP/conventional mirror switching. Modes excited by (a, b) LCP and (c, d) RCP incident on the metamaterial mirror of Figure 5 at 0.65 THz when VO_2 is in (a, c) the insulating room-temperature phase with $\sigma_{VO_2} = 10$ S/m or (b, d) the conductive high-temperature phase with $\sigma_{VO_2} = 2.6 \times 10^5$ S/m. Amplitude and phase of the magnetic field H_z is shown within the metamaterial plane as seen from the sapphire side. The instantaneous directions of currents are marked by white arrows. At low VO_2 conductivity, the resonant currents excited by circular polarizations of opposite handedness correspond to electric and magnetic dipoles, d and m. At high VO_2 conductivity, the resonant currents excited by circular polarization correspond to rotating electric dipoles.

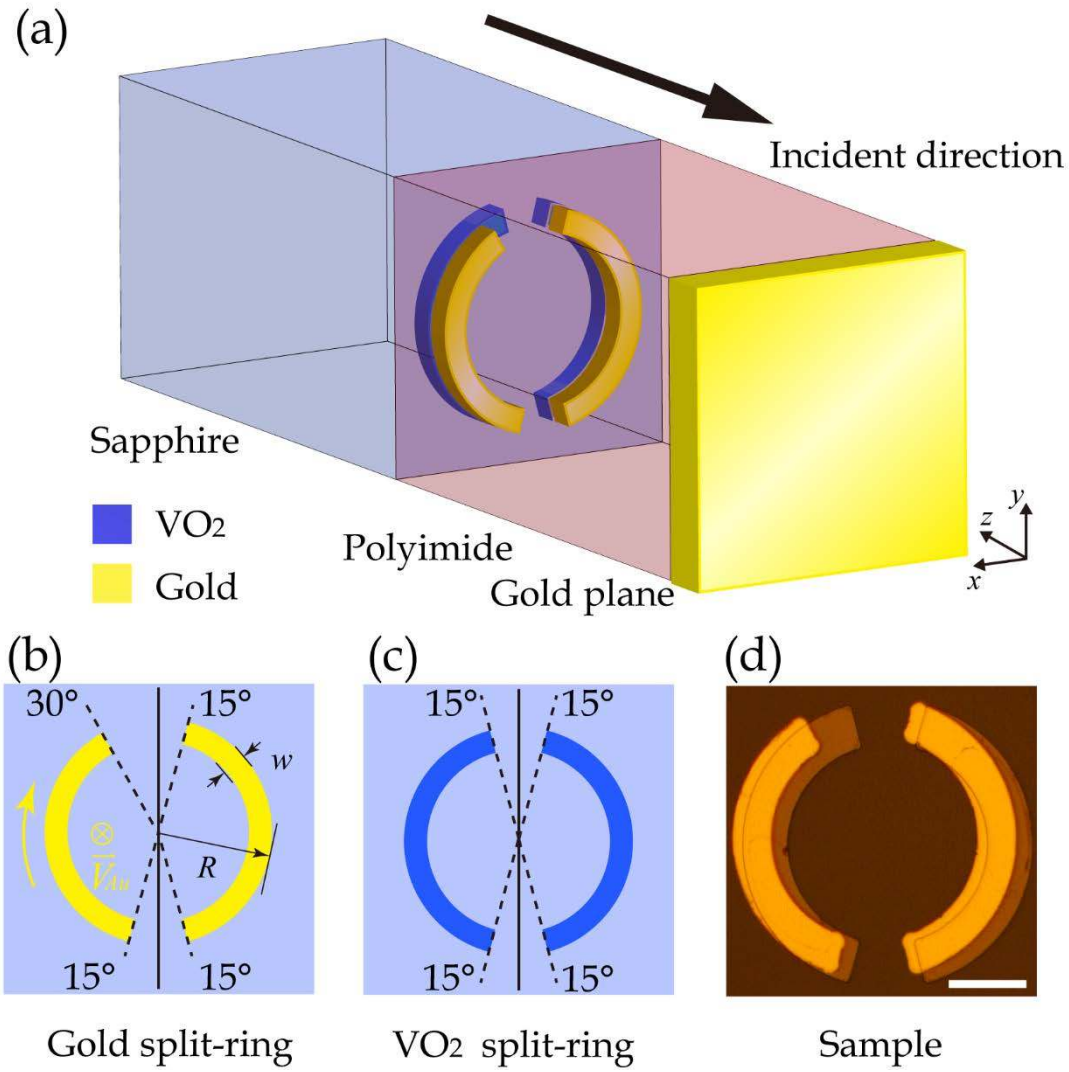

Figure 8. Switchable LCP/handedness-preserving mirror. (a) The unit cell consists of concentric and overlapping (b) asymmetrically split gold and (c) symmetrically split VO_2 rings, on a sapphire substrate, with a period of P = 80 μm, a ring radius of R = 37 μm and a ring width of w = 11 μm. The "twist vector" $\vec{V}_{Au}$ points away from the reader. A 32-μm-thick polyimide layer separates the sapphire substrate from a gold mirror. (d) Optical microscope image of the fabricated sample observed from the gold side of the ring structure with a 20 μm scale bar.

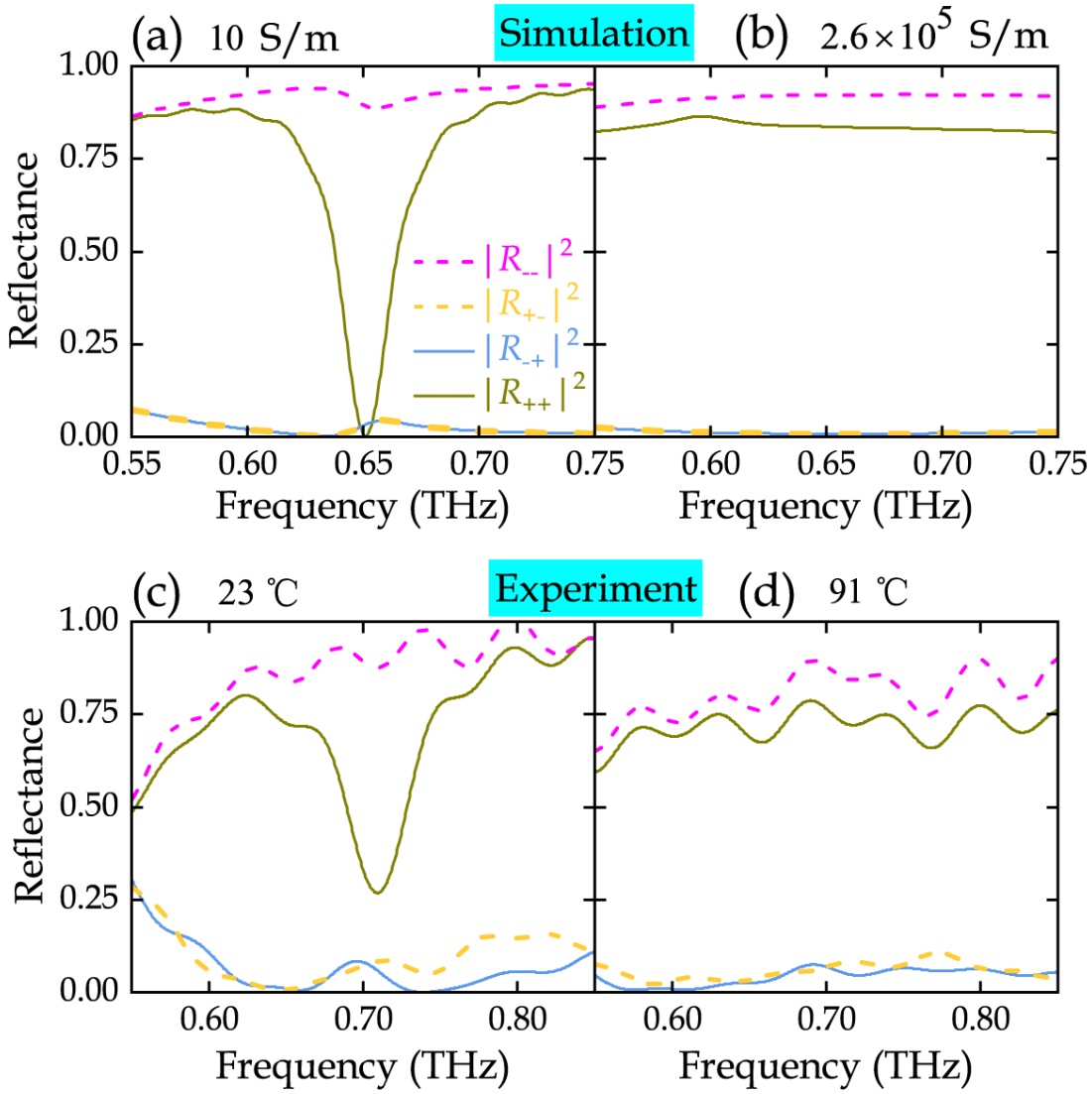

Figure 9. Switching between LCP mirror and handedness-preserving mirror based on switching VO_2 between its low-temperature insulator (left) and its high-temperature metallic (right) phases for the structure of Figure 8. Reflectance spectra in terms of circular polarization components simulated for VO_2 conductivities of (a) 10 S/m and (b) 2.6×10^5 S/m and corresponding measurements at temperatures of (c) 23 ℃ and (d) 91 ℃. (The spectral evolution with increasing conductivity of VO_2 is shown in Supplementary **Figures S9** and **S10**.)

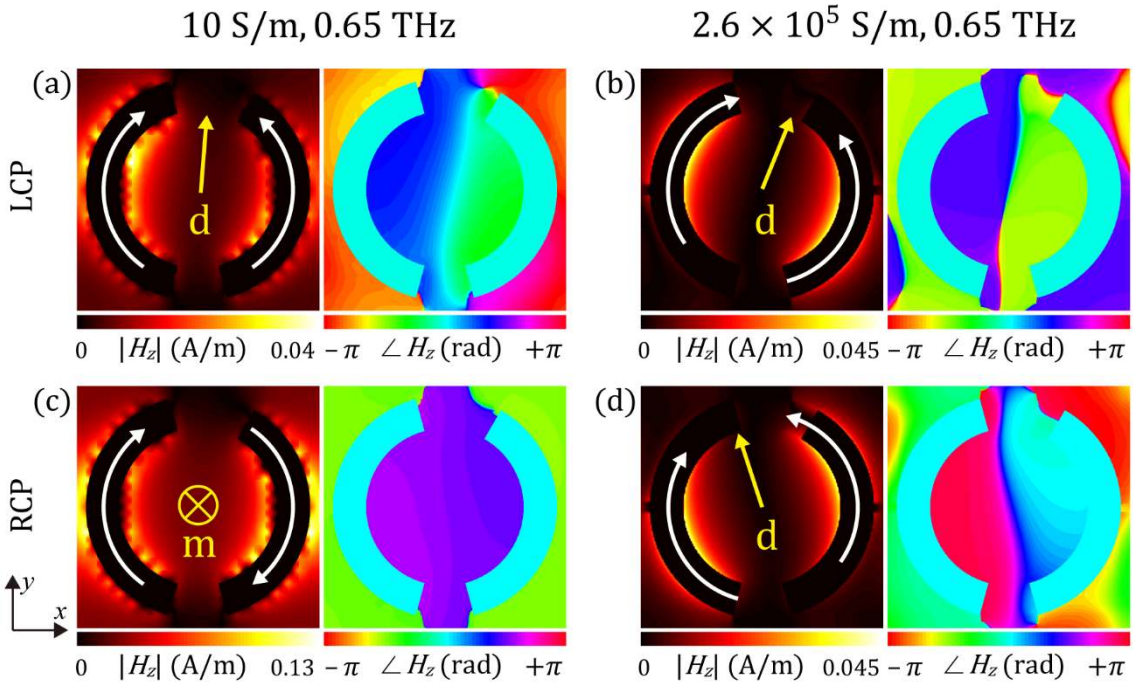

Figure 10. Physical mechanism of switching between LCP mirror and handedness-preserving mirror. Modes excited by (a, b) LCP and (c, d) RCP incident on the metamaterial mirror of Figure 8 at 0.65 THz when VO_2 is in (a, c) the insulating room-temperature phase with $\sigma_{VO_2} = 10$ S/m or (b, d) the conductive high-temperature phase with $\sigma_{VO_2} = 2.6 \times 10^5$ S/m. Amplitude and phase of the magnetic field H_z is shown within the metamaterial plane. White arrows mark the instantaneous directions of currents. At low VO_2 conductivity, the currents excited by circular polarizations of opposite handedness correspond to electric and magnetic dipoles, d and m. At high VO_2 conductivity, only electric dipole modes are excited.

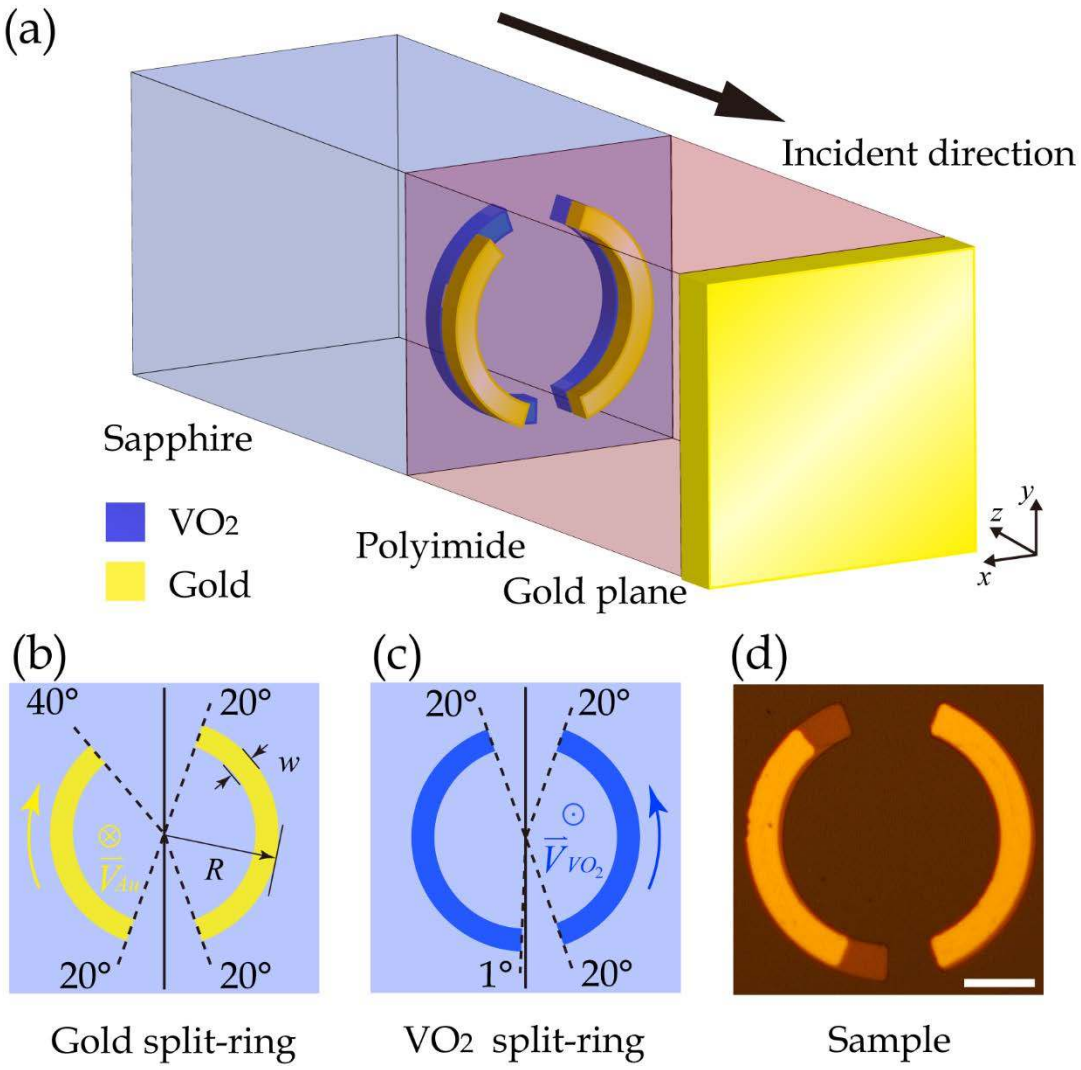

Figure 11. Switchable LCP/RCP mirror. (a) The unit cell consists of overlapping concentric asymmetrically split (b) gold and (c) VO_2 rings on a sapphire substrate, with a period of P = 88 μm, ring radius of R = 41 μm and line width of w = 10 μm. A 40-μm-thick polyimide layer separates the sapphire substrate from a gold mirror. The gap sizes and arc lengths differ as shown such that the shorter gold arc is left and the shorter VO_2 arc is right, resulting in opposite "twist vectors" $\vec{V}_{Au}$ and $\vec{V}_{VO_2}$. (d) Optical microscope image of the fabricated sample observed from the gold side of the split ring structure with a 20 μm scale bar.

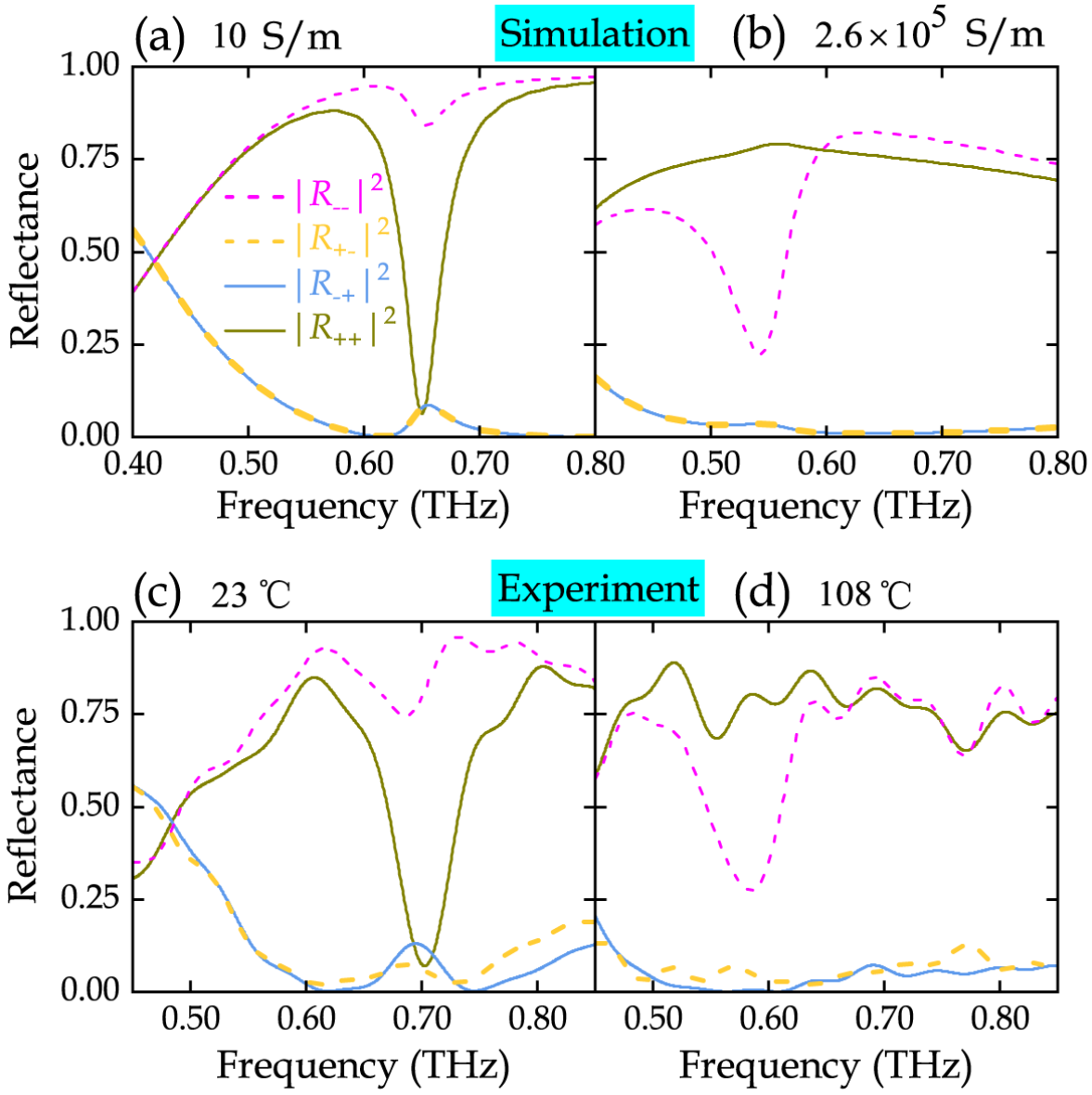

Figure 12. Switching between LCP mirror and RCP mirror based on the temperature-controlled transition of VO_2 between insulator (left) and metallic (right) phases in the metamaterial of Figure 11. Reflectance spectra simulated for VO_2 conductivities of (a) 10 S/m and (b) 2.6×10^5 S/m and corresponding measurements at temperatures of (c) 23 ℃ and (d) 108 ℃. (The spectral evolution with increasing conductivity of VO_2 is shown in Supplementary **Figures S11** and **S12**.)

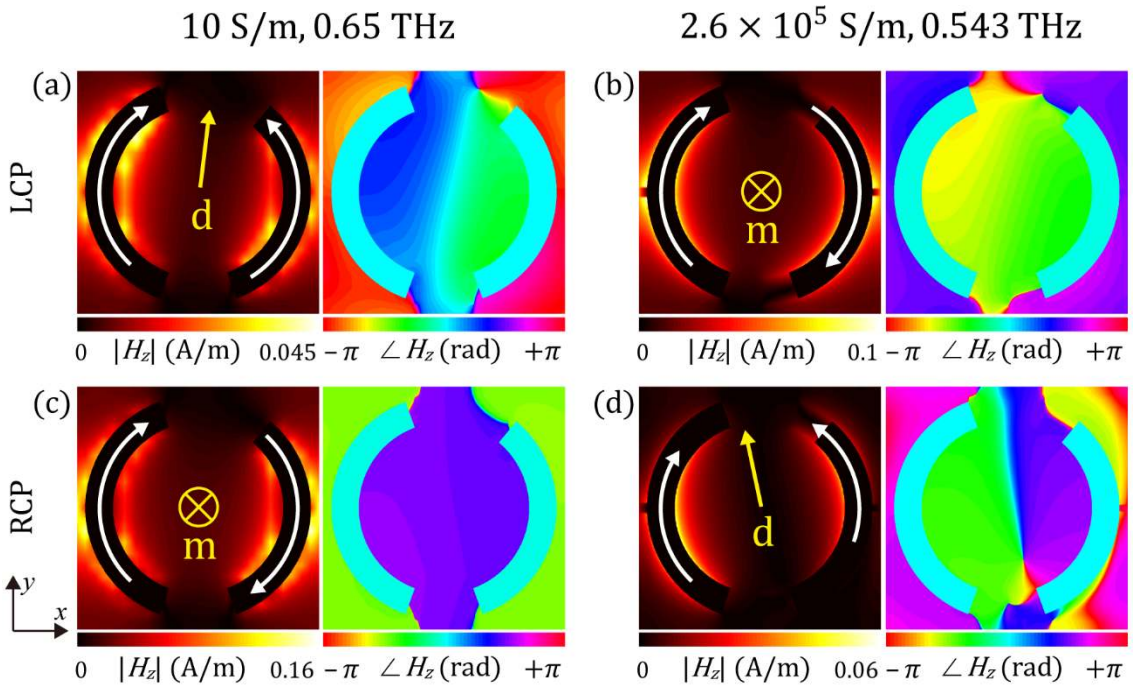

Figure 13. Physical mechanism of switching between LCP mirror and RCP mirror. Modes excited by (a, b) LCP and (c, d) RCP incident on the metamaterial mirror of Figures 11 (a, c) at 0.65 THz when VO_2 is in the insulating room-temperature phase with $\sigma_{VO_2} = 10$ S/m and (b, d) at 0.543 THz when VO_2 is in the conductive high-temperature phase with $\sigma_{VO_2} = 2.6 \times 10^5$ S/m. Amplitude and phase of the magnetic field H_z is shown within the metamaterial plane. The instantaneous directions of currents are marked by white arrows. At low VO_2 conductivity, the resonant currents excited by LCP and RCP correspond to electric and magnetic dipoles (d and m), respectively. At high VO_2 conductivity, it is the other way around.

Table of Contents Entry

Phase transitions enable active control over chirality and anisotropy of matter. We exploit this opportunity to switch electromagnetic functions of artificial materials by realizing the first switchable chiral mirrors. We demonstrate switching from a chiral mirror to either a conventional mirror, a handedness-preserving mirror, or a chiral mirror of opposite handedness.

Keyword: chirality, mirror, phase transition, circular conversion dichroism, metamaterial

Meng Liu,[#] Eric Plum,[#,*] Hua Li, Siyu Duan, Shaoxian Li, Quan Xu, Xueqian Zhang, Caihong Zhang, Chongwen Zou, Biaobing Jin, Jiaguang Han,[*] and Weili Zhang[*]

Switchable Chiral Mirrors

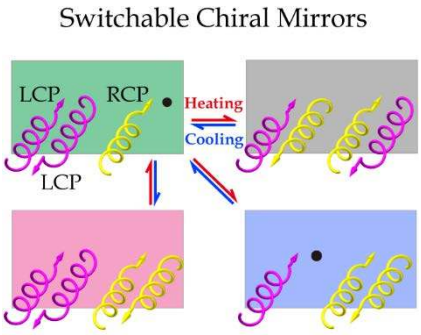

Supporting Information

Switchable Chiral Mirrors

Meng Liu,[#] Eric Plum,[#,] Hua Li, Siyu Duan, Shaoxian Li, Quan Xu, Xueqian Zhang, Caihong Zhang, Chongwen Zou, Biaobing Jin, Jiaguang Han,[*] and Weili Zhang[*]*

Properties of the VO_2 Films

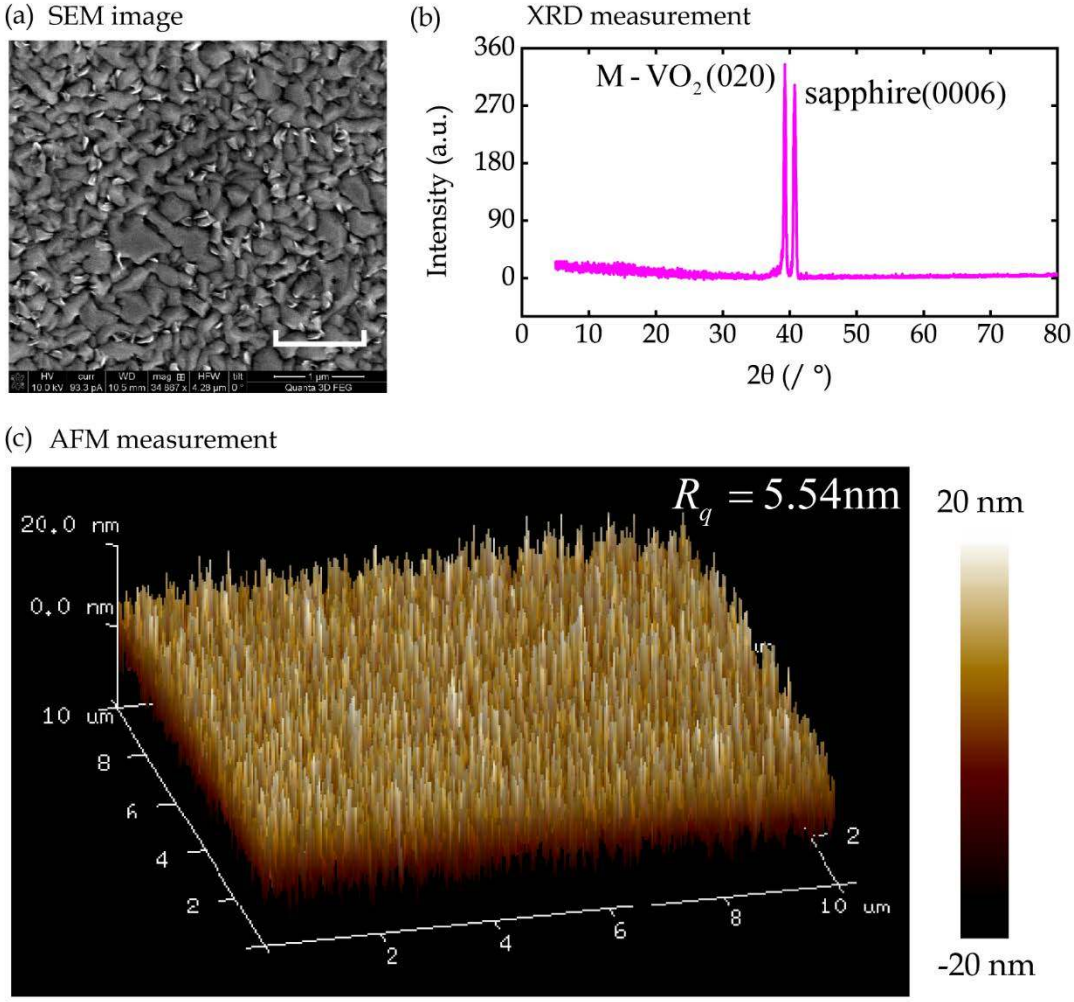

Figure S1 Measurements for 150-nm-thick VO_2 film grown on 500-μm-thick C-cut sapphire. (a) Scanning electron microscope (SEM) image with a 1 μm scale bar. (b) X-Ray Diffraction (XRD) measurement. (c) Atomic force microscope (AFM) measurement.

The fabricated 150-nm-thick crystalline VO_2 films consist of a random, semi-continuous network of nanoparticles with a mean diameter of approximately 500 nm and voids (Fig. S1a). Room-temperature x-ray diffraction (XRD) measurements reveal intensity peaks at angles 2θ of 39.2° and 41.3°, indicating crystalline VO_2 and sapphire, respectively (Fig. S1b). Our VO_2 films exhibit a single monoclinic structure with preferred orientation of (020) at room temperature. According to atomic force microscopy (AFM), the root-mean-square (RMS) surface roughness of the films is R_q = 5.54 nm, which is small compared to their thickness (Fig. S1c).

A THz time-domain spectroscopy (THz - TDS) system has been employed to measure the conductivity of a typical VO_2 film in the 23-102 ℃ temperature range. The fabricated VO_2/sapphire sample was then fixed to a thermo-electric heater/cooler which has an aperture of 1.5cm×1.5cm at the center. Transmission measurements were performed in a drying chamber in a frequency range of 0.2–2.0 THz for THz waves normally incident on the "VO_2" side of the sample with a beam diameter of approximately 5 mm. All presented THz transmission spectra were normalized to spectra of the substrate.

The measured temperature-dependence of transmission and conductivity of the VO_2 film (Fig. S2) at 0.65 THz reveals the insulator-to-metal phase transition at the characteristic temperature of 68 ℃. Transmission at room temperature of 23 ℃ is almost unity (0.9995), corresponding to a low conductivity of σ_{VO_2}= 40 S/m and the insulating monoclinic crystal structure of VO_2 (left inset). The film's transmission decreases dramatically as the film is heated across the phase transition temperature, corresponding to a similarly dramatic increase

in conductivity. At temperatures of 65-75 ℃, the VO_2 film has a mixture of insulating monoclinic crystal structure and metallic rutile crystal structure. At 102 ℃, the film's transmission drops to 0.21 and its conductivity reaches $\sigma_{VO_2} = 2.6\times10^5$ S/m, indicating that the film is fully switched to the metallic rutile crystal structure of VO_2 (right inset).

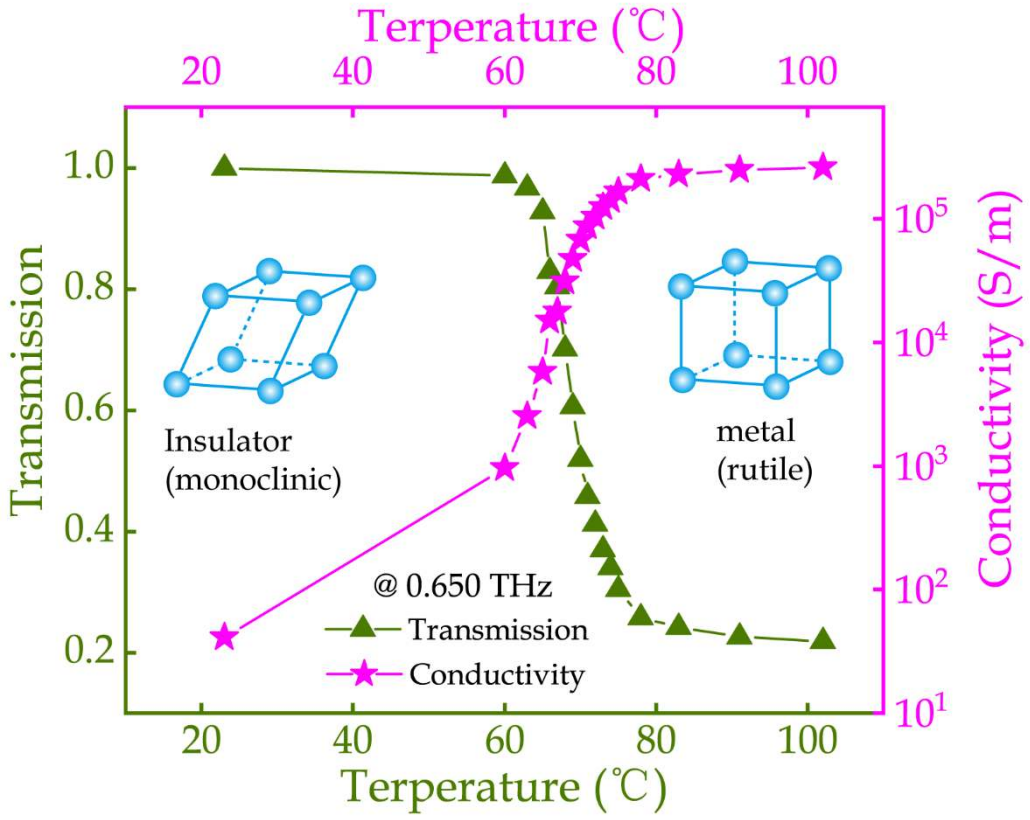

Figure S2 Measured temperature-dependence of transmission and conductivity of 150-nm-thick VO_2 film at a frequency of 0.65 THz.

Switching Circular Conversion Dichroism

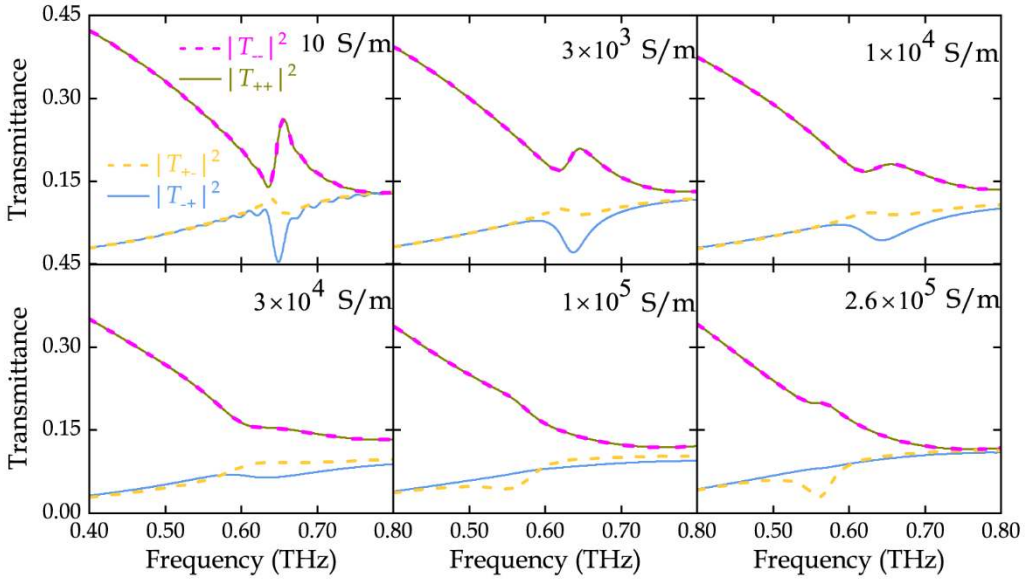

Figure S3 Switching of circular conversion dichroism illustrated by simulated transmittance spectra of the metamaterial of article Fig. 2 for different conductivities of VO_2 in terms of intensity for right-handed (+) and left-handed (-) circularly polarized waves illuminating the split rings from the sapphire side. Direct transmittance corresponds to $|T_{++}|^2$, $|T_{--}|^2$ and conversion corresponds to $|T_{-+}|^2$, $|T_{+-}|^2$.

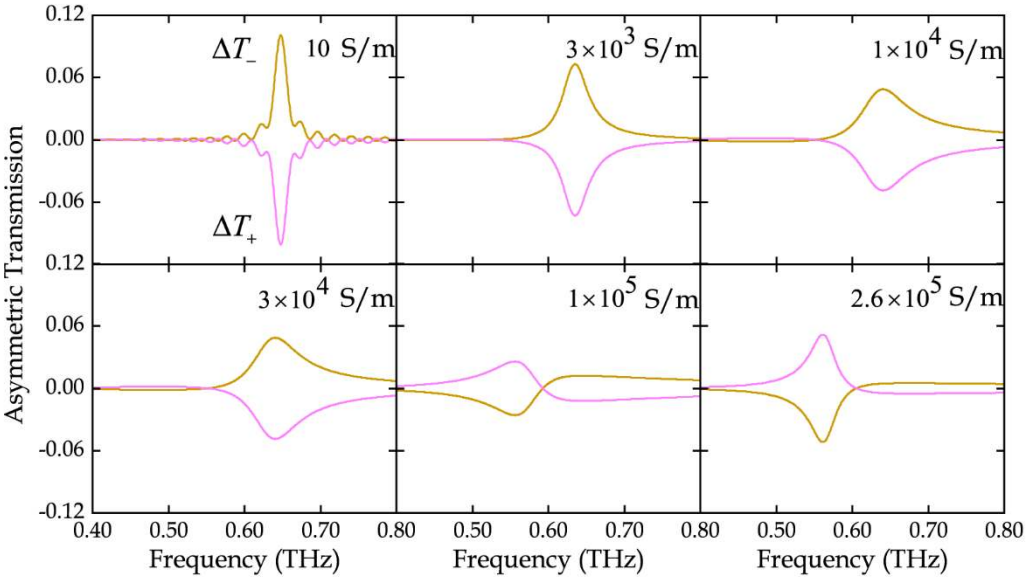

Figure S4 Asymmetric transmission spectra of the metamaterial of article Fig. 2 for different conductivities of VO_2 (calculated from Fig. S3).

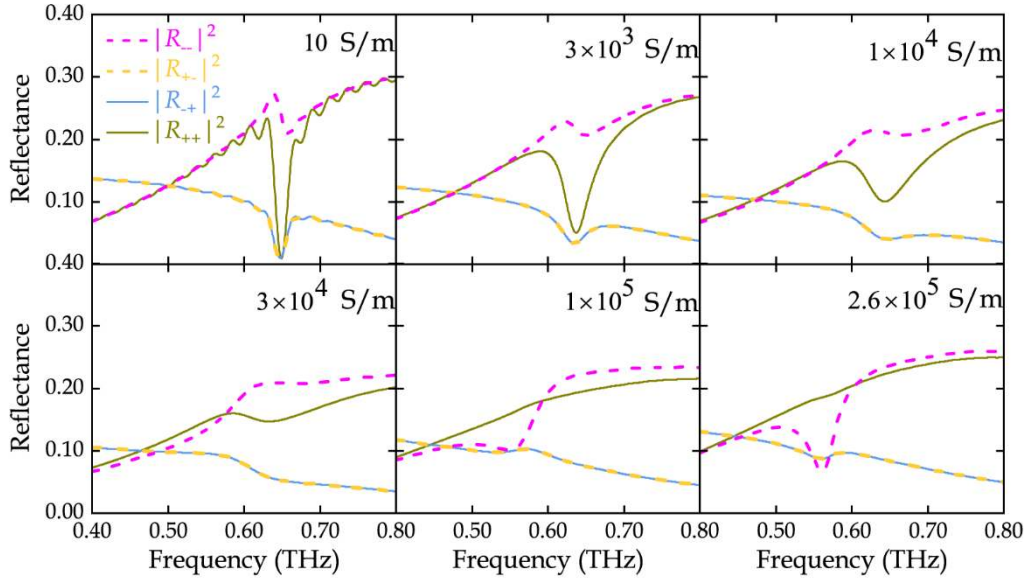

Figure S5 Switching of circular conversion dichroism illustrated by simulated reflectance spectra of the metamaterial of article Fig. 2 for different conductivities of VO_2. Direct reflectance corresponds to $|R_{-+}|^2$, $|R_{+-}|^2$ and conversion corresponds to $|R_{++}|^2$, $|R_{--}|^2$.

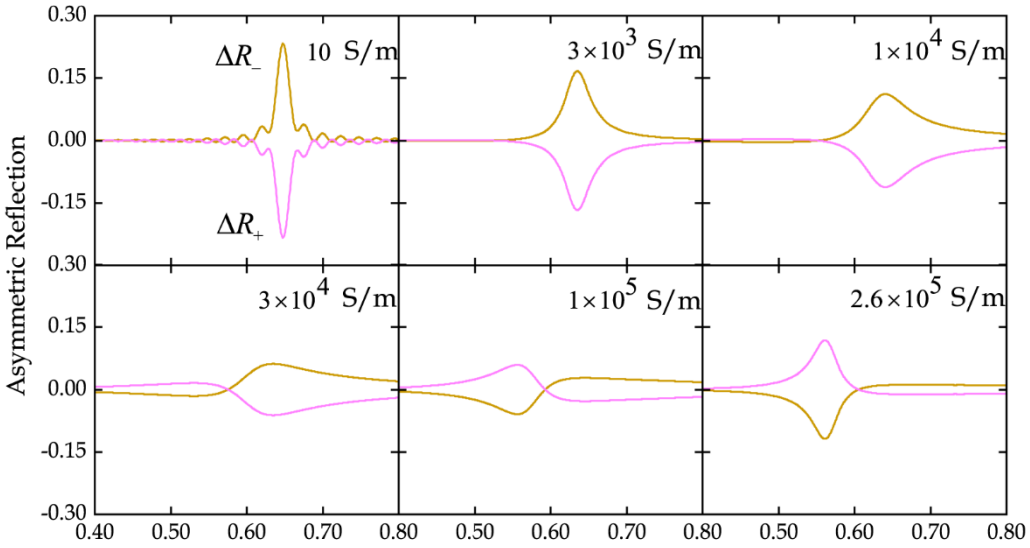

Figure. S6 Asymmetric reflection spectra of the metamaterial of article Fig. 2 for different conductivities of VO_2 (calculated from Fig. S5).

Transition between Chiral Mirror and Conventional Mirror

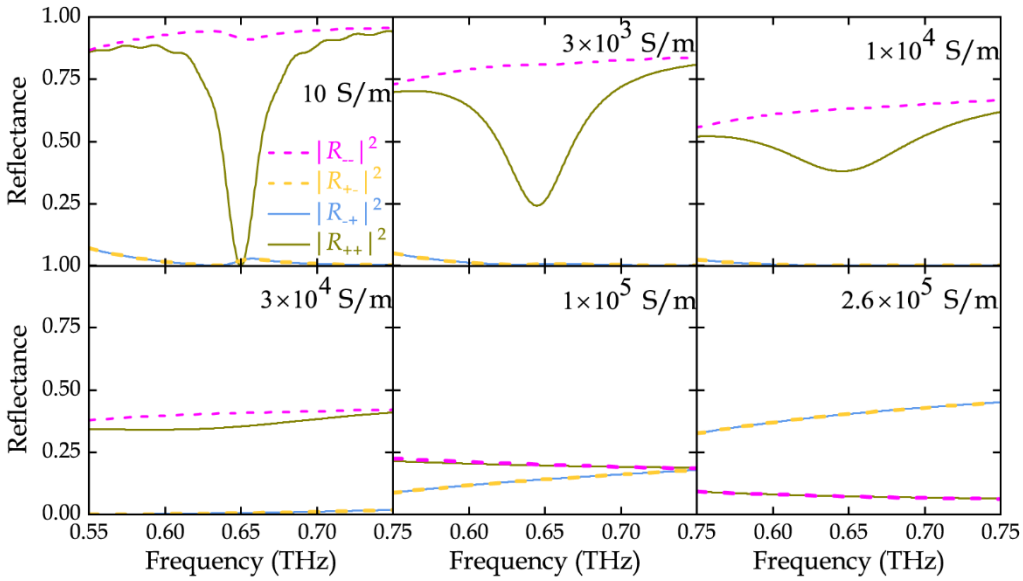

Figure S7 Transition between LCP mirror and conventional mirror illustrated by simulated reflectance spectra of the mirror of article Fig. 5 for different VO_2 conductivities.

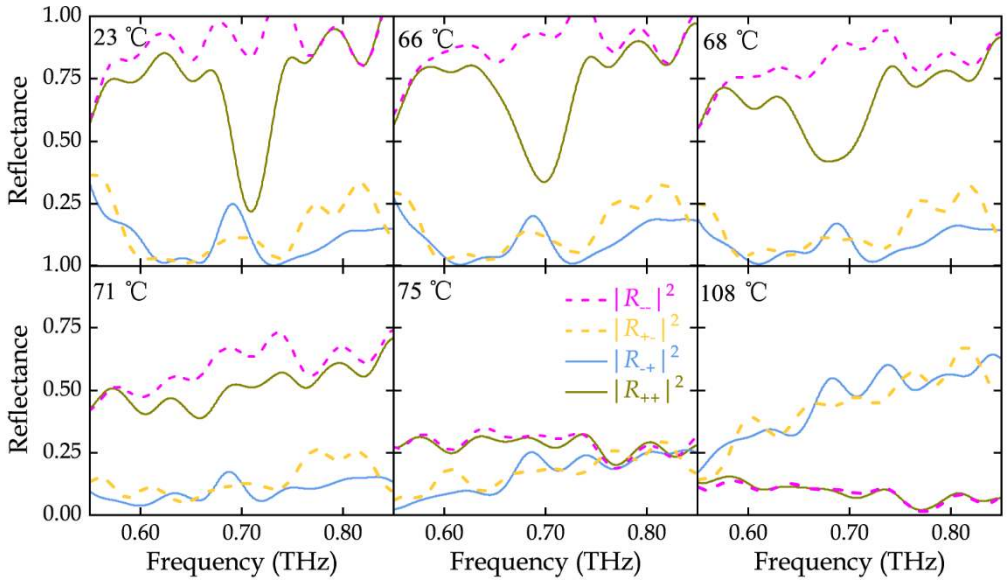

Figure S8 Transition between LCP mirror and conventional mirror illustrated by measured reflectance spectra of the mirror of article Fig. 5 at different temperatures.

Transition between LCP Mirror and Handedness-preserving Mirror

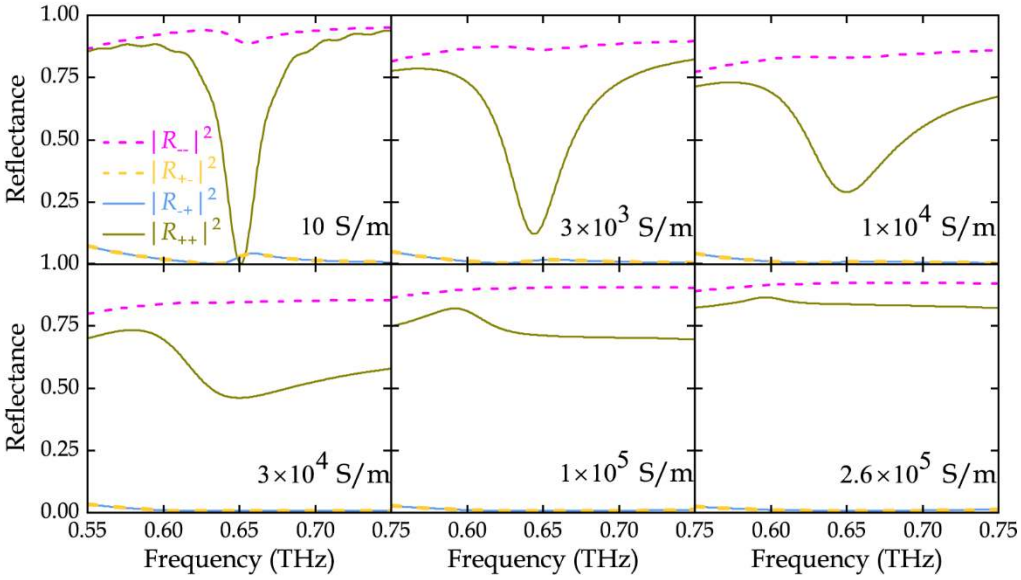

Figure S9 Transition between LCP mirror and handedness-preserving mirror illustrated by simulated reflectance spectra of the mirror of article Fig. 8 for different VO_2 conductivities.

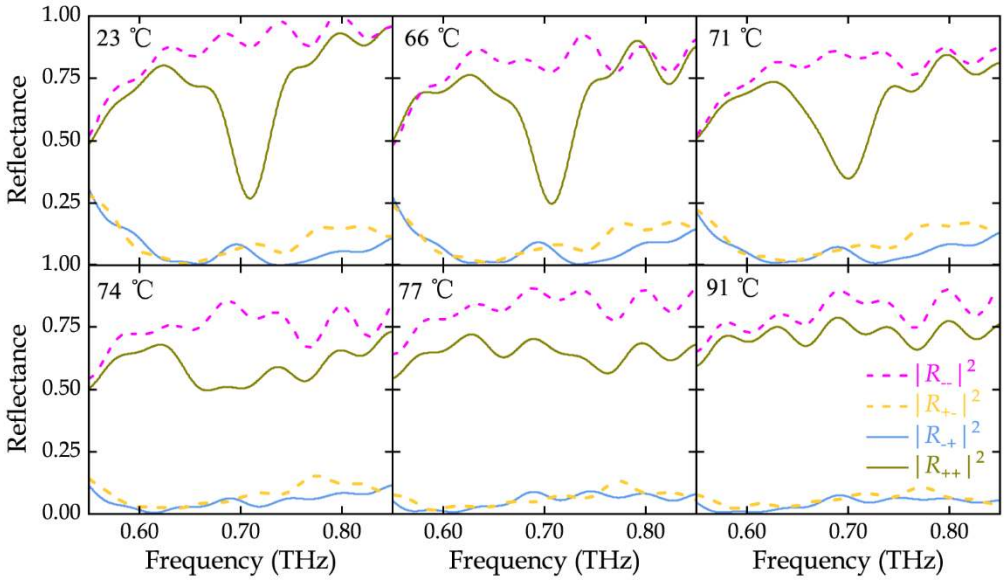

Figure S10 Transition between LCP mirror and handedness-preserving mirror illustrated by measured reflectance spectra of the mirror of article Fig. 8 at different temperatures.

Transition between LCP Mirror and RCP Mirror

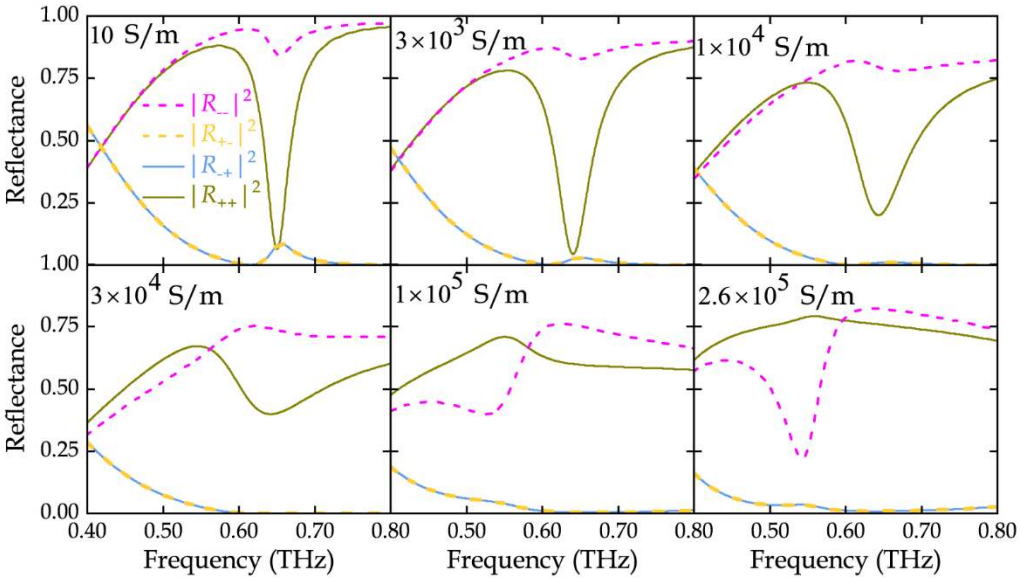

Figure S11 Transition between LCP mirror and RCP mirror illustrated by simulated reflectance spectra of the mirror of article Fig. 11 for different VO_2 conductivities.

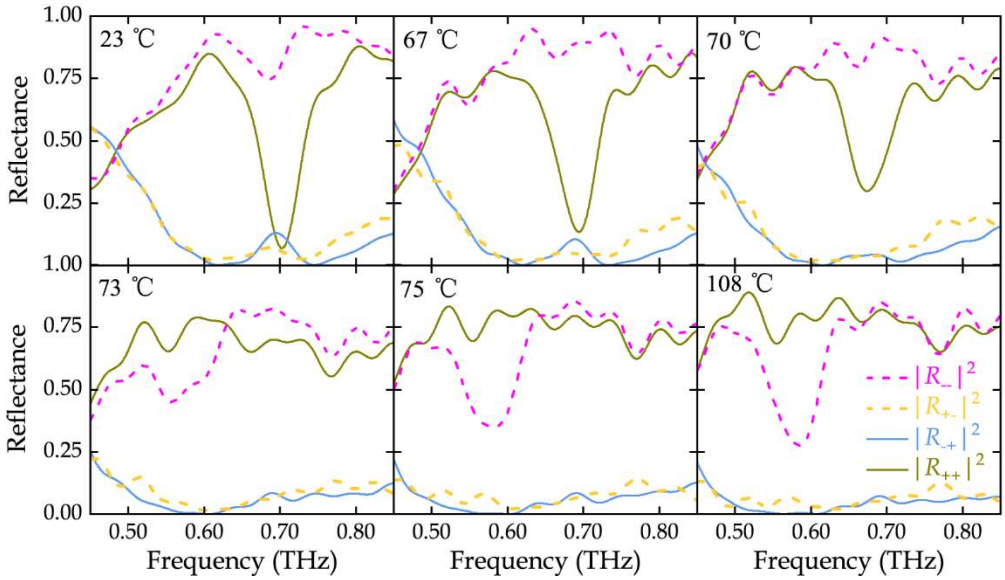

Figure S12 Transition between LCP mirror and RCP mirror illustrated by measured reflectance spectra of the mirror of article Fig. 11 at different temperatures.